Fluid-assisted metasomatic processes on planetary bodies: Evidence from vestan lithologies

T Shisseh, H Chennaoui Aoudjehane, Jean-Alix Barrat, Brigitte Zanda, Roger H. Hewins, C B Agee, L Folco, Emmanuel Jacquet, Sylvain Pont

To cite this version:

T Shisseh, H Chennaoui Aoudjehane, Jean-Alix Barrat, Brigitte Zanda, Roger H. Hewins, et al.. Fluid-assisted metasomatic processes on planetary bodies: Evidence from vestan lithologies. Geochimica et Cosmochimica Acta, 2022, 340, pp.51 - 64. 10.1016/j.gca.2022.11.007 . hal-04636773

METASOMATIC PROCESSES RECORDED IN VARIOUS VESTAN LITHOLOGIES: CASE STUDY OF NORTHWEST AFRICA 11911, 1664, 8675 AND 13269

Authors: T. Shisseh[a], H. Chennaoui Aoudjehane[a], J. A. Barrat[b], B. Zanda[c], R. H. Hewins[c], C. Agee[d], L. Folco[e], E. Jacquet[c], S. Pont[c]

[a]Hassan II University of Casablanca, Faculty of Sciences Ain Chock, GAIA Laboratory, km 8 Route d'El Jadida 20150 Casablanca, Morocco

[b]Université Européenne de Bretagne and CNRS UMR 6538, U.B.O-I.U.E.M., 29280 Plouzané Cedex, France

[c]Laboratoire de Minéralogie et Cosmochimie du Muséum, MNHN and CNRS UMR 7202, 75005 Paris, France

[d]Institute of Meteoritics, University of New Mexico, Albuquerque, NM 87131, USA.

[e]Dipartimento di Scienze della Terra, Università di Pisa, V. S. Maria 53, 56126 Pisa, Italy

ABSTRACT:

Fe-rich secondary phases found in the polymict eucrite NWA (Northwest Africa) 11911, the howardite NWA 1664, the monomict eucrite NWA 8675 and the unbrecciated basaltic eucrite NWA 13269 were investigated to elucidate their origin and history of formation. NWA 11911 is the only rock that displays widespread Fe-enrichment near fractures in unequilibrated and slightly equilibrated basaltic clasts and pyroxene fragments. Fayalitic olivine veinlets with various textures, thicknesses and compositions (Fa_{64-82}) are detected in unequilibrated pyroxenes in NWA 11911, NWA 1664 and NWA 8675. Neighbouring Fe-enriched pyroxene is also Al-depleted ($Al_2O_3 \approx 0.3$ wt%). Despite a careful search, NWA 13269 seems to lack Fe-enrichment in pyroxene and ferroan olivine, but contains Ca-rich plagioclase (An_{97-98}) veinlets associated with Cr-spinel. Olivine veinlets have been also detected in equilibrated pyroxene in NWA 11911. Our observations support the circulation of hydrothermal fluids throughout the fractures of eucritic material. These findings are also consistent with the detection of gullies, pitted terrains, and water-rich carbonaceous material on the surface of (4) Vesta by the Dawn spacecraft.

1. INTRODUCTION

Howardites, eucrites and diogenites (HED) form the largest achondrites suite recovered from Earth's surface. Eucrites are upper crust samples, and are basaltic and gabbroic rocks formed as lava flows or magmatic intrusions. Diogenites are lower crust samples, and they are mostly orthopyroxenites, and occasionally harzburgitic, dunitic or noritic rocks. Howardites consist of both eucritic and diogenitic lithologies, and often comprise exogenous contaminants (Zolensky et al., 1996; Gounelle et al., 2003; Lorenz et al., 2007; Janots et al., 2012; Beck et al., 2012; Shirai et al., 2016; Unsalan et al., 2019; Yesiltas et al., 2019). Hubble telescope observations and spectroscopic mapping data from NASA's Dawn mission, have provided important clues linking the HED to the protoplanet (4) Vesta (Binzel et al., 1997; McSween et al., 2013; Russell et al., 2013; De Sanctis et al., 2013; Ammannito et al., 2013).

Dawn has also revealed the presence of low-albedo, carbon- and water-rich material within or in close proximity of impact craters, or scattered throughout the surface of the asteroid (McCord et al., 2012; Reddy et al., 2012). Further mapping data led to the discovery of OH-bearing minerals (De Sanctis et al., 2012; Nathues et al., 2014), exogenous hydrogen (Prettyman et al., 2012), pitted terrains and gullies respectively formed by the degassing of volatiles and water flow (Denevi et al., 2012; Scully et al., 2015).

The petrogenetic history of HED meteorites did not stop after crystallization from their parent magmas. Post-magmatic processes on their parent body include (1) metamorphism (Takeda and Graham, 1991; Metzler et al., 1995; Yamaguchi et al., 1996, 1997; Yamaguchi, 2000). (2) multiple brecciation events (Metzler et al., 1995; Kennedy et al., 2019). (3) Various types of metasomatism (Duke and Silver, 1967; Treiman et al., 2004; Barrat et al., 2011; Chen et al., 2015; Mayne et al., 2016; Warren et al., 2014, 2017; Zhang et al., 2013, 2018, 2020). Among the latter is Fe-metasomatism, which has been detected in few eucrites and eucritic clasts in howardites, resulting in Fe-enrichment along the fractures in pyroxene and the precipitation of fayalite, Ca-rich plagioclase, Cr-spinel, troilite and apatite and/or merrillite (Takeda et al., 1983, 1994; Warren, 2002; Mittlefehldt and Lindstrom, 1997; Barrat et al., 2011; Roszjar et al., 2011; Warren et al., 2014; Mayne et al., 2016; Pang et al., 2017; Patzer and McSween, 2018; Vollmer et al., 2020).

Several scenarios have been suggested to explain the occurrence of such Fe-rich, secondary features in eucritic material. Takeda et al. (1983, 1994) and Warren (2002) suggested a short duration heating event (~1100 ºC) which caused melting of late-stage, Fe-rich mesostasis that was subsequently deposited within the fractures in pyroxene. Alternatively, Roszjar et al. (2011) proposed that pyroxene incongruently melted to produce Fe-rich olivine and plagioclase in a magma chamber. Barrat et al. (2011), on the other hand, suggested that these features formed during the circulation of a metasomatic Fe-rich fluid throughout the fractures of host eucritic rocks. They also established the following three-stage scheme to characterize the degree of metasomatism:

Stage 1: Pyroxenes with Fe-enrichment along the fractures, often filled with olivine inclusions.

Stage 2: Cracks in pyroxene filled with fayalitic veinlets associated with minor Ca-rich plagioclase and troilite.

Stage 3: Occurrence of Al-depleted and Fe-enriched pyroxene accompanied by well-developed olivine and secondary plagioclase veinlets

In this study, we investigate the petrological and compositional variation engendered by secondary alteration in four, distinct lithologies from the upper crust of Vesta. This includes NWA 11911, NWA 1664, NWA 8675 and NWA 13269. We also discuss the plausible origin of the secondary products in light of what have been previously published in the literature, and their implication for the complex evolution of the Vestan crust.

2. MATERIALS AND METHODS

Polished sections of NWA 11911, NWA 1664, NWA 8675 and NWA 13269 were subjected to study using the scanning electron microscopes TESCAN VEGAII LSU at IMPMC-MNHN (Paris, France) and FEI Quanta 450 ESEM FEG with (EDS) Bruker QUANTAX XFlash Detector 6-10 at the University of Pisa (Pisa, Italy) in backscattered electron mode at an accelerating voltage of 15 kV. Chemical compositions of pyroxene, plagioclase, silica and oxides were obtained using CAMECA SX-FIVE at ISTeP-Sorbonne University (Paris, France) and further analysis were performed using JEOL 8200 Super Probe at the University of Milan (Milan, Italy) and the Institute of Meteoritics at the University of New Mexico (Albuquerque, USA). An accelerating voltage of 15 kV and a beam current of 10 nA were used during the analyses. To effectively track the petrographical changes in the pyroxene crossed by secondary phases, we performed FeO, MgO, CaO, Al2O_3, TiO_2, Cr_2O_3 profiles across Mg-rich, dark cores, Fe-enriched pyroxenes and fayalitic veinlets. EPMA-WDS and EDS maps have also been generated.

3. RESULTS

3.1 PETROGRAPHY AND MINERAL COMPOSITION

NWA 11911

This rock is brecciated and comprises clasts exhibiting a wide range of textures (variolitic, subophitic, ophitic and granulitic textures; Fig. S1). The main minerals are plagioclase and pyroxene, with ilmenite, silica, chromite, troilite, Fe-Ni metal and olivine as minor phases. Unequilibrated and equilibrated pyroxene fragments and clasts with various sizes are present within the lithic, well-cemented matrix. The compositions of low-Ca pyroxene have an average of $En_{39\pm4}Fs_{54\pm7}Wo_{7\pm6.7}$ (n = 39). The average composition of high-Ca pyroxene is $En_{29\pm2.2}Fs_{35\pm7}Wo_{36\pm6.4}$ (n = 17). Plagioclase has a maximum size of 1 mm, and exhibits a compositional range of $An_{72-93}Ab_{6-26}Or_{1-2}$ (n = 22).

This meteorite also contains an impact melt (~5×3 mm²) exhibiting a vitrophyric texture. This large clast consists of a glassy matrix enclosing zoned pyroxene microlites (40-80 µm; $En_{44-49}Fs_{44-48}Wo_{7-8}$) and partially digested pyroxene and plagioclase minerals with remelted rims. Shock veins are up to 300 µm in width, they are glassy and contain rounded to subrounded pyroxene, plagioclase and silica fragments. The clast shown in Fig. S2 consists of host augite ($Fs_{27-32}Wo_{40-42.5}$), stubby fayalitic olivine (~Fa_{77}) and silica lamellae (0.8 wt% FeO) up to 10 µm in width, as well as plagioclase (An_{74-83}). Some regions have pyroxene ($En_{39}Fs_{58}Wo_{1.9}$) associated with 1 µm-sized troilite and scarce olivine (see also false-color EDS maps in Fig. S2).

NWA 13269

This rock is unbrecciated and exhibits a distinct porphyritic texture (Fig. S3). Pyroxene phenocrysts up to 2.5 mm long are embedded in a fine-grained, subophitic to variolitic groundmass. Pyroxene in the matrix is equilibrated, and contains augite exsolution lamellae up to 1.5 µm in width with an interval of about 5 µm. Pyroxene phenocrysts have an average composition of $En_{47\pm1.9}Fs_{51\pm1.6}Wo_{2\pm0.7}$ (n = 15). Low-Ca pyroxene in the groundmass is pigeonite, exhibiting a compositional range of $En_{39-41}Fs_{42-53}Wo_{5.4-17.5}$ (n = 3). High-Ca pyroxene has an average composition of $En_{36\pm1.9}Fs_{27\pm8}Wo_{37\pm9.8}$ (n = 9). Plagioclase laths (300 µm long) are clouded, and have a composition ranging from $An_{78}Ab_{12}Or_{10}$ (K_2O = 1.5 wt%) to $An_{89}Ab_{10}Or_1$ (K_2O = 0.2

wt%). Mesostasis consisting of silica, ilmenite and troilite is abundant, and mostly occurs between plagioclase laths.

NWA 1664 AND NWA 8657

The main petrological characteristics of NWA 1664 (howardite) and NWA 8657 (monomict eucrite) have been previously described in the literature (Kurat et al., 2003; Lorenz et al., 2007; Barrat et al., 2009; Barrat et al., 2012; Ruzicka et al., 2014).

3.2. FE-ENRICHMENT IN PYROXENE

NWA 11911 is the only sample in this study that comprises abundant pyroxene fragments and clasts displaying Fe-enrichment in close proximity of the fractures (Fig. 1). These can be subdivided as follows.

Unequilibrated pyroxene fragments

Pyroxene fragments shown in Fig. 1a, 1b display Fe-enrichment along the fractures, which often affects the Mg-cores resulting in parallel BSE-lighter bands. Tiny BSE-bright phases are often detected within the fractures (Fig. 1a). Fe-enrichment in pyroxene is extended to up to 17 µm toward the Mg-cores. The compositions of dark, Mg-rich cores are En_{58-63} Fs_{32-35} Wo_{5-7}. Fe-enriched pyroxene near the fractures have compositions ranging from $En_{38}Fs_{56}Wo_6$ to $En_{37}Fs_{60}Wo_3$ (Table 1; Fig. 1).

Unequilibrated basaltic clasts

Few lithic (basaltic) clasts that are scattered throughout the matrix of NWA 11911 show comparable features. A basaltic clast (~1.5 mm large) exhibiting a subophitic texture is presented in Fig. 1c. It mainly consists of unequilibrated pyroxene, 40 µm-sized plagioclase laths (An_{86-89}) and minor mesostasis composed of silica, olivine, ilmenite and troilite. Fe-enrichment in host pyroxene is only observed in the lower right part of the clast despite the homogenous distribution of the fractures, and is extending to up to 10 µm inward. Healed fractures are also observed. Compositions range from $En_{55}Fs_{37}Wo_8$ within the cores to $En_{42}Fs_{55}Wo_3$ in Fe-enriched pyroxene near the cracks (Table 1). The clast fragment shown in Fig. 1d has also a subophitic texture, but lacks mesostasis. The plagioclase is up to 80 µm in width, and has a composition of An_{88-93}. The chromite grain (30 µm) between plagioclase laths is $Chr_{60}Usp_{3}Spl_{36}$. Pyroxene exhibits Mg-Fe zoning, and displays Fe-enrichment in cracks extending to up to 20 µm inward. Mg-cores have compositions of $En_{61}Fs_{33}Wo_{6,}$ whereas Fe-enriched host pigeonite, adjacent to cracks, has a composition of $En_{40}Fs_{54}Wo_{6}$. Tiny high-Ca exsolution lamellae (< 1 µm) are detected in both pristine and metasomatized pyroxene (see the close-up view in Fig. 1d). Inclusions of olivine (~1 µm) are found filling a fracture located in the lower part of the clast.

Slightly equilibrated pyroxene fragments

Several pyroxene grains in NWA 11911 exhibit exsolution of (>1 µm) augite lamellae, but partially preserve their Mg-Fe zoning and display Fe-enrichment in cracks. The pyroxene fragment shown in Fig. 1e is up to 400 µm in size, and contains 2 µm-thick augite lamellae spaced by up to 7 µm. Mg-cores are $En_{51}Fs_{43}Wo_{6}$, and the Fe-enriched pyroxenes adjacent to the fractures are $En_{42}Fs_{52}Wo_{6}$ (Table 1). The composition of the rim is $En_{40}Fs_{50}Wo_{10}$, indicating magmatic Ca-zoning. Inclusions composed of plagioclase (1.5 FeO wt%), silica, troilite and chromite are detected within some of the Fe-rich areas in pyroxene (see the close-up images in Fig. 1e). Another slightly equilibrated pyroxene fragment comprising two types of Ca-rich exsolution lamella is presented in Fig. 1f. The first ones ($En_{33}Fs_{27}Wo_{40}$) are 7 µm-thick with an interval of about 30 µm, and are locally displaced by up to 13 µm due to faulting of host pyroxene. The second exsolved lamellae occur between the former. They are discontinuous with a width not exceeding 1 µm. The remnant Mg-cores are 20 µm in diameter and have compositions of $En_{48-49}Fs_{45-46}Wo_{4-5}$ (Mg# = 0.5). The composition of Fe-enriched pyroxene is $En_{39-42}Fs_{55}Wo_{3-6}$ (Mg# = 0.4) (Table 1).

3.3. FAYALATIC VEINLETS AND ASSOCIATED PHASES

Unequilibrated pyroxene fragments and basaltic clasts

NWA 11911

In addition to Fe-enriched pyroxene fragments and clasts in NWA 11911, we also detected fragments of pyroxene exhibiting Fe-enrichment along cracks that are filled with fayalite, Ca-rich plagioclase, Cr-spinel, troilite and apatite (Fig. 2; additional SEM images and EPMA profiles are presented in Fig. S4, S5 in the online supplement).

Pyroxene fragment shown in Fig. 2a consists of dark cores ($En_{61}Fs_{34}Wo_5$), Fe-rich rims ($En_{39}Fs_{54}Wo_7$) and Fe-enriched areas ($En_{39}Fs_{58}Wo_3$) near the fractures and olivine veinlets. Some of these veinlets (5 µm thick) consist of granular olivine, continuous Ca-rich plagioclase veinlets, chromite and troilite (Fig. 2b). Olivine in these veinlets is often surrounded by uncommon Ca-rich areas. The composition of olivine in the rim is Fa_{78} and changes to Fa_{75} in the interior of the fragment (Table 1). Ca-rich plagioclase, often associated with ferroan olivine filling cracks, have a composition of An_{96-98} (with FeO =1.2 wt%) (Table 1). Cr-spinel mostly occur within veinlets and exhibit a compositional range of $Chr_{70-72}Usp_{5-8}Spl_{19-20}$ (Fe^{3+}/Fe^{2+} = 0.029-0.041). Using the compositions of Cr-spinel and olivine and the method of Wlotzka (2005), the estimated equilibration temperatures are 753 ± 9.7 ºC (Table 3). Troilite up to 10 µm in size mostly occurs in the rim of the pyroxene fragment, but decrease in size and abundance toward the interior. We measured FeO, MgO, CaO, Al_2O_3, Cr_2O_3, TiO_2 profiles across the veinlet (marked A-B in Fig. 2b). CaO content (wt%) vary due to the presence of tiny high-Ca exsolution lamellae (<3 µm) in pyroxene (Fig. 2c). The Al_2O_3 content is up to 1.2 wt% in the Mg-core, but decreases gradually toward the olivine veinlet (0.3 wt% Al_2O_3).

The compositional ranges of olivine veinlets shown in Fig. S4 are Fa_{73-77}. The Mg-core of host pyroxene has a composition of $En_{60}Fs_{35}Wo_5$. The Fe-enriched pyroxene adjacent to veinlets is $En_{40}Fs_{54}Wo_6$, and does not exhibit the Al-depletion detected in the previous fragment.

NWA 1664

Some of the unequilibrated clasts and pyroxene fragments in NWA 1664 are excessively invaded by a complex network of olivine veinlets. Associated phases are secondary plagioclase, Cr-spinel, troilite and plausibly silica (Fig. 3; see also Fig. S6). The 1-mm-sized, subophitic clast shown in Fig. 3a consists of clouded plagioclase laths (200 µm in width), zoned pyroxenes with Mg-cores up to 70 µm in diameter as well as minor ilmenite and silica. Fe-enrichment in pyroxene extends into the magnesian cores by a distance of 15 µm. Olivine is present within pyroxene in the form of 10-µm-thick veinlets or patches up to 40 µm across. The veinlets are often displaced due to fracturing and faulting of host pyroxene (Fig. 3a). Plagioclase is frequently penetrated by veinlets in close vicinity of the faulting area.

Pervasive veining of host, Mg-rich pyroxene is also observed in the subophitic clast shown in Fig. 3b. Note the presence of intact mesostasis areas between plagioclase laths, and the occurrence of vermicular olivine and silica within the Fe-rich rim of pyroxene. In this clast, Fe-enrichment in pyroxene is limited, extending into the magnesian cores by a distance of 3 µm only. The thickness of fayalitic veinlets ranges from 1 to up to 60 µm. These are continuous and often comprise fragments of pyroxene that most likely have sheared off from the host pyroxene walls (see the close-up view in Fig. 3b). In several areas, the fayalitic veinlets penetrate or cross the primary plagioclase. Note that, interestingly, the veinlets crossing plagioclase are mostly dominated by troilite.

The fayalitic veinlets shown in Fig. 3c and Fig. 3d are 6-8 µm thick, and are associated with Ca-rich plagioclase, Cr-spinel and troilite. The veinlet shown in Fig. 3d is texturally comparable to some of the veinlets found in NWA 1109, where Cr-spinel occurs between olivine layers (Pang et al. 2017). Note that pyroxene host comprises fine and parallel, Ca- and Cr-rich exsolution lamellae. The former mostly lack in the areas adjacent to olivine veinlets, suggesting that Ca was leashed before or after the metamorphic event that triggered the exsolution.

Olivine in NWA 1664 is less ferroan, and have a composition of Fa_{66} (Table 2). Mg-cores compositions are $En_{70}Fs_{28}Wo_2$. The Fe-enriched margins in close proximity of the olivine veinlets have compositions of $En_{42}Fs_{57}Wo_1$. Primary plagioclase is An_{81-90} (FeO = 0.2-0.9 wt%), whereas secondary plagioclase is An_{97-98} (FeO = 1.4 wt%) (Table 2). Cr-spinel associated with olivine veinlets exhibits a compositional range of $Chr_{50-64}Usp_{4-10}Spl_{20-21}$ (Fe^{3+}/Fe^{2+} = 0.028-0.031). Equilibration temperatures of Cr-spinel and olivine are ranging from 759 to 851°C.

EPMA profiles across olivine veinlets and EPMA-WDS maps are presented in Fig. 4, Fig. S6 and Fig. S7. Pyroxene near cracks filled with olivine is Al-depleted, with Al_2O_3 ranging from 1.4 wt% in pristine cores to 0.3 wt% in metasomatized regions. The concentrations of CaO and Cr_2O_3 increase in some areas, and decrease in others. Note that no significant variation in TiO_2 content is detected.

NWA 8675

The pyroxenes in the monomict eucrite NWA 8675 exhibit comparable secondary features (Fig. 5; Fig. S8). The thickness of fayalitic veinlets ranges from 5 µm, within the interior of pyroxene, to up to 40 µm at the pyroxene-plagioclase boundaries. Olivine exhibits a compositional range of Fa_{78}-$_{80}$. The composition of Mg-cores is up to $En_{60}Fs_{35}Wo_5$. Metasomatized pyroxene adjacent to veinlets is very Fe-rich, and have a composition of $En_{28}Fs_{71}Wo_1$. Mg-rich cores are penetrated by BSE-white and parallel, Fe-rich bands up to 2 µm in width. Primary plagioclase is An_{86-95} (FeO = 0.7 wt%). Secondary plagioclase, on the other hand, contains up to 1.5 wt% FeO, and have and end-member composition of An_{97-98} (Table 2). An EPMA profile measured across pyroxene displaying Fe-enrichment and contains olivine veinlets filling fractures is illustrated in Fig. 6. The increase of Cr_2O_3 content toward the core represents magmatic zoning. Metasomatized pyroxene in this eucrite exhibits the lowest Al_2O_3 concentrations (0.2 wt%) measured in this study.

Equilibrated pyroxene fragments

NWA 11911

We report here the occurrence of olivine veinlets in an equilibrated pyroxene fragment in NWA 11911 (Fig. 7; see also EDS maps and EPMA profiles given in Fig. S9). Host pigeonite is $En_{35}Fs_{55}Wo_{10}$ and exhibits parallel, 1 µm-thick augite exsolution lamellae. These are often bended or displaced by a distance of 1 µm. Pyroxene near the veinlet is slightly Fe-enriched, and have a composition of $En_{33}Fs_{59}Wo_8$ (Fs_4 variation). Olivine in the veinlet exhibits a compositional range of Fa_{72-80}. Occasionally, unusual Ca-rich areas are detected between the host pyroxene and veinlet boundaries. Note the occurrence of rounded to subrounded, exsolved pyroxene fragments (~2 µm) within the veinlet. This indicates that deposition of olivine postdates the thermal event that caused equilibration of this fragment.

3.4. SECONDARY PLAGIOCLASE VEINLETS

NWA 13269

Despite a careful search, neither Fe-enrichment in pyroxene nor ferroan olivine veinlets are detected in NWA 13269. However, this meteorite contains highly Ca-rich plagioclase veinlets ($An_{97}Ab_{3;}$ FeO wt% = 0.83; Table 2) comprising inclusions of Cr-spinel ($Chr_{67.8\pm1.7}Usp_{22.8\pm2.7}Spl_{7\pm1.6}$; $Fe^{3+/}Fe^{2+}$ = 0.035; n = 3) and troilite (Fig. 8). Ca-rich plagioclase veinlets within the pyroxene phenocrysts (exhibiting Cr-rich lamellae) and pyroxene in the groundmass (with Ca-rich lamellae) are shown in Fig. 8a. Note the abrupt change of the orientation of the veinlets when crossing the mineral boundaries. The veinlet shown in Fig. 9b is 6 µm thick, and contains rounded Cr-spinel inclusions up to 3 µm in size. In some areas, secondary plagioclase is absent and only continuous or discontinuous chromite veinlets are observed.

4. DISCUSSION

4.1. ORIGIN FROM A COMMON PARENT BODY

The concentration of Fe and Mn (atom per formula unit) of pyroxene in planetary basalts appears to be correlated with the distance from the sun (Papike 1998). Fe/Mn ratios in pyroxene increases following this sequence Vesta-Mars-Earth-Moon. All the pyroxenes in this study, including those who are affected by secondary alteration, follow the trend line of (4) Vesta, implying a common origin for our samples (Fig. S10).

4.2. FORMATION OF THE SECONDARY VEINLETS

NWA 11911, NWA 1664 and NWA 8675 show evidence of brecciation and exhibit a wide range of textures and compositions. These rocks, in addition to the unbrecciated eucrite NWA 13269, have also been subjected to various degrees of thermal metamorphism as indicated by the exsolution of augite from host pigeonite and the clouding of major mineral phases (Harlow and Klimentidis, 1980; Yamaguchi et al., 1996). The brecciated samples exhibit Fe-enriched, unequilibrated and slightly equilibrated pyroxenes that comprise fractures filled with secondary fayalite, nearly pure anorthite, Cr-spinel, troilite and apatite (Tables 1 and 2; Fig. 2, 3, 5, 7, 8, 9 and 10; see also the chemical summary presented in Table S1 and S2). These features correspond to Barrat et al. (2011)'s stage 2 and stage 3 of secondary alteration. The first stage, characterized by Fe-enrichment along the fractures in pyroxene, was exclusively detected in NWA 11911 (Fig. 1). NWA 13269, on the other hand, seems to lack these Fe-rich features, and only comprises anhortitic veinlets and Cr-spinel instead. Affected pyroxenes in NWA 11911, NWA 1664 and NWA 8675 are compositionally following the Mg-Fe-Ca or Mg-Fe trends, typically consistent with metamorphic type 2 and type 3 pyroxenes in Takeda and Graham (1991) and Schwartz and McCallum (2005) schemes, respectively (Fig. 9). The magmatic zoning of pyroxenes that comprise Ca-rich plagioclase veinlets in NWA 13269 was slightly to completely erased by metamorphism (type 4-5 in Takeda and Graham (1991) scheme), resulting in the exsolution of augite in pigeonite marked by the Fe-Ca trend (Fig. 9).

The features observed in these rocks have been most likely formed during a post-magmatic, secondary process in the upper crust of their parent body. We exclude an exogenic, terrestrial or magmatic origin for the following reasons: (1) The Fe/Mn ratio of Fe-enriched pyroxene and olivine veinlets filling cracks in pyroxene and clasts are matching the ratios reported in HED meteorites (Fig. S10). (2) Olivine has never been reported as a weathering product in hot desert finds. The only weathering product identified here is calcite (Fig. 3, Fig. 6), which has been previously found filling fractures in weathered meteorites (Barrat et al., 2003; Crozaz et al., 2003). (3) Magmatic olivine in Vestan meteorites exhibits Mg-rich compositions Fa_{7-39} (Beck et al., 2012; Mittlefehldt, 2015; Vaci et al., 2021), whereas olivine found in mesostasis or formed by decomposition of Fe-rich pyroxene is ranging from Fa_{72} to Fa_{86} (Takeda and Graham, 1991; Patzer and McSween, 2012). NWA 11911 contains an augitic clast comprising olivine (Fa_{76}). Neither Fe-enrichment of pyroxene nor the phases associated with the fayalitic veinlets described above are detected. In addition, the texture of olivine is broadly different from the veinlets, and resemble some of the late-stage assemblages described in the work of Patzer and McSween (2012) (see their Fig. 1b).

Several scenarios have been suggested to explain the occurrence of such features in eucritic meteorites. These are discussed below in light of our findings.

Impact reheating of mesostasis and injection into pyroxene fractures

In an attempt to reveal the origin of ferroan olivine veinlets in the eucrite Yamato (Y)-7501, Takeda et al. (1983, 1994) suggested that they formed either during a process of Fe-rich pyroxene decomposition, or during a short impact heating event (~1100 ºC) that caused melting of late-stage, Fe-rich mesostasis. The resulted melts would have been subsequently deposited within the pyroxene fractures (see also Warren (2002)). Barrat et al. (2011) argued against such a mechanism, given that they found neither a relationship between the fayalitic veinlets and mesostasis, nor evidence of its melting in their samples. According to reheating experiments on eucritic material, melting of mesostasis would produce liquids enriched in P, K, Ti, Th and REEs (Yamaguchi and Mikouchi, 2005; Barrat et al., 2007; Yamaguchi et al., 2013). This implies that, if these melts infiltrated pyroxene, an enrichment in Ti and REEs would be expected. Barrat et al. (2011) inspected the REE concentration of Fe-enriched pyroxene in the polymict eucrite NWA 049 and reported that the Fe-enriched and Mg-cores in pyroxene are compositionally similar in terms of their REEs content. In addition, no Ti enrichment in pyroxene has been detected. Thus, following these observations, the scenario involving melting of mesostasis and injection in pyroxene fractures has been ruled out, since it could not account for the formation of the secondary, Fe-rich features observed in few eucritic lithologies.

Our findings strongly support this latest view since we find neither evidence of melting of mesostasis, nor Ti enrichment in pyroxene. For instance, the mesostasis domains found in the Fe-enriched clasts in NWA 11911, and the fayalite-bearing clasts in NWA 1664 are well preserved and are not linked to any of the Fe-rich features (Fig. 2c, Fig. 4b). The Fe-rich rims in these clasts often exhibit a vermicular texture, and contain inclusions of olivine and silica indicating decomposition of metastable pyroxene (see Patzer and McSween, 2012). Yet they do not show any indication of remelting or connection to the Fe-enriched margins near the fractures and the fayalitic veinlets. We have also compared the concentrations of Ti in Fe-enriched and pristine pyroxenes (Fig. 11; see also EPMA profiles in Fig. 2, 4, 6 and Fig. S4, S7), and we did not detect any striking Ti enrichment in the former. It should be noted that the increase of Ti/Al ratio observed in Fe-enriched pyroxene is not due to a higher Ti abundances, but is a result of Al-depletion (stage 3 in Barrat et al. (2011) scheme).

Incongruent melting in a magma chamber

When Roszjar et al. (2011) reported the occurrence of Fe-enriched pyroxene and fayalitic veinlets associated with chromite, troilite and apatite in the Stannern-trend eucrite NWA 5073, they suggested an alternative scenario involving incongruent melting of pyroxene in a magma chamber. During this process, pyroxene would have been heated slightly above the solidus at a temperature of 1150 ºC (Stolper, 1977) and incongruently melted to produce ferroan olivine and Ca-rich plagioclase. Chromite, on the other hand, would have a magmatic origin and may have been simply incorporated in the veinlets. Although this scenario successfully explains the occurrence of olivine in pyroxene but not in plagioclase, as well as the presence of chromite within the veinlets, it fails to account for the presence of veinlets in both zoned and homogenized pyroxenes, as well as the occurrence of troilite and apatite in association with olivine, since they mostly form during the last stage of the crystallization of the magma (Sarafian et al., 2013; Pang et al., 2017; Vollmer et al., 2020).

In our samples, although in rare cases, we discovered plagioclase crossed or slightly penetrated by fayalitic veinlets (Fig. 3b). The Fe-enrichment in pyroxene and the olivine veinlets occur in pyroxenes with a wide range of compositions. In addition, we found troilite and apatite incorporated within the veinlets. These observations strongly argue against the incongruent melting scenario. Recent heating experiments by Rombeck et al. (2021) showed that pyroxene develops Fe-Ti-rich phases at a temperature of 1070 ºC. However, instead of exhibiting Fe-enrichment, pyroxene adjacent to these phases became Fe-depleted. This contradicts our results and strongly argues against a heating event as the sole responsible process for the formation of Fe-rich phases in the studied eucritic material. However, it might explain the occurrence of Fe-rich bands and Cr exsolution lamellae observed in some pyroxenes (Fig. 3, Fig. 5, Fig. 8, Fig. S5; see also Pang et al. (2017)).

Interaction with a metasomatic fluid

Another scenario for the origin of secondary Fe-rich phases involves the circulation of a metasomatic, Fe-rich fluid throughout the fractures of host eucritic rocks (Mittlefehldt and Lindstrom, 1997; Schwartz and McCallum, 2005; Barrat et al., 2011; Warren et al., 2014).

Based on work from Schwartz and McCallum (2005), Fe-enrichment along the fractures in the polymict eucrite Pasamonte, which is comparable to that observed in NWA 11911, is the result of an interaction between the rock and an Fe-rich vapor. However, although the coexistence of solids and high temperature vapors (> 1300 ºC) is possible (Dohmen et al., 1998), Barrat et al. (2011) showed that this scenario is inconsistent with the physical and chemical conditions of the upper crust of Vesta; accordingly, they favored an aqueous nature of the fluid.

Water deposits in the form of a quartz veinlet were previously reported in the cumulate eucrite Serra de Magé (Treiman, 2004). Aqueous fluids may have existed during early magma crystallization as evidenced by the detection of OH-rich apatite in eucrites (Sarafian et al., 2013, 2017; Barrett et al., 2016), or delivered during the collisions of Vesta with cometary or carbonaceous bodies (Treiman et al., 2004; Warren et al., 2014). This latter suggestion is strongly supported by the discovery of exogeneous, carbonaceous material within howardites and polymict eucrites (Zolensky et al., 1996; Gounelle et al., 2003; Lorenz et al., 2007; Janots et al., 2012; Beck et al., 2012; Shirai et al., 2016; Unsalan et al., 2019; Yesiltas et al., 2019), and on the surface of (4) Vesta as revealed by Dawn data (McCord et al., 2012; Reddy et al., 2012; De Sanctis et al., 2012).

Warren et al. (2014) suggested that aqueous fluids may have been generated during a the collision of a carbonaceous, water-rich impactor (likely CM chondritic) with Vesta. The mixing of carbonaceous material with the Vestan regolith and further impacts may have contributed to their further mobilization. This is in agreement with the detection of water activity on the surface of (4) Vesta, indicated by the presence of gullies and pitted terrains within crater walls and floors (Denevi et al. 2012; Scully et al. 2015). Following this view, it would be possible that the FeO-metasomatic features described above are the result of the circulation of aqueous fluids throughout the preexisting fractures in the various studied eucritic lithologies (Fig. 12).

Recent hydrothermal experiments showed that Fe-rich phases in pyroxene form whether the interacting liquid originally contained Fe or not (Rombeck et al., 2021). This suggests that the metasomatic agent may not have been predominantly Fe-rich as previously thought, and plausibly exhibited compositional variations (by dissolution/precipitation) as it percolates throughout the fractures of eucritic material. The fluid may have been gradually enriched in Ca and Al, as indicated by the absence of Ca-rich lamellae in close proximity of the veinlets (Fig. 3c, d), as well as the Al-depletion in pyroxene. This could provide an explanation to why NWA 13269 only comprises secondary plagioclase veinlets and inclusions of Cr-spinel, but lack the Fe-rich features reported in the remaining samples. However, we cannot rule out that these missing features (at least Fe-enrichment in pyroxene) may have been erased by subsequent metamorphism. The effects of later metamorphism and further impact events are shown by the healing of the fractures, the presence of exsolution lamellae and Ca-rich areas enclosing the fayalitic veinlets (Fig. 2) in pyroxene, as well as fracturing and faulting of pyroxene hosts causing the displacement of the veinlets (Fig. 3a).

Fluid-assisted secondary alteration has been also suggested to explain the formation of olivine veinlets associated with secondary plagioclase and Cr-spinel in Apollo 14 samples and a limited number of lunar meteorites (Arai et al., 2010; Warren, 2018; Zeng et al., 2020). However, differently from HED meteorites, the metasomatic fluids are suggested to be from an endogenic origin. Note that, at present, an endogenic source for the fluids forming secondary alteration features in eucrites cannot also be ruled out (Sarafian et al., 2013, 2017; Barrett et al., 2016).

5. CONCLUSIONS

We rigorously explored the petrography and the geochemistry of eucritic clasts and pyroxene fragments exhibiting Fe-enrichment and crossed by fayalitic olivine veinlets in four distinct lithologies from Vesta in order to constrain the processes involved in their formation. These lithologies include the polymict eucrite NWA 11911, the howardite NWA 1664, the monomict eucrite NWA 8675 and the unbrecciated eucrite 13269. Fe-enrichment in pyroxene is not restricted to unequilibrated pyroxenes, but was also found in some slightly equilibrated fragments in NWA 11911. Olivine within the veinlets exhibits a wide range of compositions, with the least ferroan olivines are found in NWA 1664. The veinlets also comprise various proportions of Ca-rich plagioclase, Cr-spinel, troilite and apatite. Differently from the other samples, Fe-enrichment in pyroxene and Fe-rich phases were not detected in NWA 13269, as its veins solely consists of secondary plagioclase and Cr-spinel. Geochemical profiles across metasomatized pyroxenes show Al-depletion in close vicinity of the veinlets, with the exception of one pyroxene fragment in NWA 11911. Ca-depletion is also observed as evidenced by the abrupt lack of exsolution lamellae within adjacent pyroxene.

The formation of secondary phases in eucritic material is most likely the result of circulation of aqueous fluids within the upper Vestan crust, combined with multiple heating events (global crustal metamorphism and impacts). The source of these fluids is still debated, and might be endogenic or brought to the surface by impacts. In all cases, the detection of these features shed more light on the complex evolutionary history of the crust of Vesta, and constitutes further evidence of the presence and the delivery of water to the surface of presumably dry small bodies.

6. ACKNOWLEDGMENTS

We thank Luc Labenne and Didi Baidari for providing pieces of NWA 11911 and NWA 13269 for classification at the MNHN in Paris and the Institute of Meteoritics at the University of New Mexico, respectively. We also wish to thank Jean-Alix Barrat for providing samples of NWA 1664 and NWA 8675. The analyses were performed during the mobilities that were funded by the Erasmus+ program to the Natural History Museum of Paris in France for a period of seven months, and to the University of Pisa in Italy for a period of five months. Further analyses have been performed during a one year mobility that was funded by the Fulbright joint supervision program at to the the institute of Meteoritics (University of New Mexico) in USA. We kindly appreciate the constructive comments of David W. Mittlefehldt and Justin Simon. This work is a part of the ATTARIK Foundation for promoting Meteoritics and Planetary Science in Morocco, Arab countries and Africa www.attarikfoundation.org.

REFERENCES

Ammannito E., De Sanctis M. C., Palomba E., Longobardo A., Mittlefehldt D. W., McSween H. Y., Marchi S., Capria M. T., Capaccioni F., Frigeri A., Pieters C. M., Ruesch O., Tosi F., Zambon F., Carraro F., Fonte S., Hiesinger H., Magni G., McFadden L. A., Raymond C. A., Russell C. T., and Sunshine J. M. (2013) Olivine in an unexpected location on Vesta's surface. *Nature* **504**, 122–125.

Arai T., Hawke B. R., Giguere T. A., Misawa K., Miyamoto M., and Kojima H. (2010) Antarctic lunar meteorites Yamato-793169, Asuka-881757, MIL 05035, and MET 01210 (YAMM): Launch pairing and possible cryptomare origin. *Geochim. Cosmochim. Acta* **74**, 2231–2248.

Barrat J. A., Jambon A., Bohn M., Blichert-Toft J., Sautter V., Göpel C., Gillet Ph., Boudouma O., and Keller F. (2003) Petrology and geochemistry of the unbrecciated achondrite Northwest Africa 1240 (NWA 1240): An HED parent body impact melt. *Geochim. Cosmochim. Acta* **67**, 3959–3970.

Barrat J. A., Yamaguchi A., Greenwood R. C., Bohn M., Cotten J., Benoit M., and Franchi I. A. (2007) The Stannern trend eucrites: Contamination of main group eucritic magmas by crustal partial melts. *Geochim. Cosmochim. Acta* **71**, 4108-4124.

Barrat J. A., Bohn M., Gillet P., and Yamaguchi A. (2009) Evidence for K- rich terranes on Vesta from impact spherules. *Meteor. Planet. Sci.* **44**, 359-374.

Barrat J. A., Yamaguchi A., Bunch T. E., Bohn M., Bollinger C., and Ceuleneer G. (2011) Possible fluid–rock interactions on differentiated asteroids recorded in eucritic meteorites. *Geochim. Cosmochim. Acta* **75**, 3839-3852.

Barrat J. A., Yamaguchi A., Jambon A., Bollinger C., and Boudouma O. (2012) Low-Mg rock debris in howardites: Evidence for KREEPy lithologies on Vesta?. *Geochim. Cosmochim. Acta* **99**, 193-205.

Barrett T., Barnes J., Tartèse R., Anand M., Franchi I., Greenwood R., Charlier B., and Grady M. (2016) The abundance and isotopic composition of water in eucrites. *Meteor. Planet. Sci.* **51**, 1110–1124.

Beck A. W., Welten K. C., McSween Jr H. Y., Viviano C. E., and Caffee M. W. (2012) Petrologic and textural diversity among the PCA 02 howardite group, one of the largest pieces of the Vestan surface. *Meteor. Planet. Sci.* **47**, 947-969.

Binzel R. P., Gaffey M. J., Thomas P. C., Zellner B. H., Storrs A. D., and Wells E. N. (1997) Geologic mapping of Vesta from 1994 Hubble space telescope images. *Icarus* **128**, 95-103.

Boyce J. W., Tomlinson S. M., McCubbin F. M., Greenwood J. P., and Treiman A. H. (2014) The lunar apatite paradox. *Science* **344**, 400-402.

Chen H. Y., Miao B. K., and Huang L. L. (2015) Ancient silicification on asteroid 4 Vesta: Evidence from a eucrite Grove Mountains (GRV) 13001 from Antarctic. *Meteor. Planet. Sci.* **50**, #5003 (abstract).

Crozaz G., Floss, C. and Wadhwa M. (2003) Chemical alteration and REE mobilization in meteorites from hot and cold deserts. *Geochim. Cosmochim. Acta* **67**, 4727-4741.

Denevi B. W., Blewett D. T., Buczkowski D. L., Capaccioni F., Capria M. T., De Sanctis M. C., Garry W. B., Gaskell R. W., Le Corre L., Li J.-Y., Marchi S., McCoy T. J., Nathues A., O'Brien D. P., Petro N. E., Pieters C. M., Preusker F., Raymond C. A., Reddy V., Russell C. T., Schenk P., Scully J. E. C., Sunshine J. M., Tosi F., Williams D. A., and Wyrick D. (2012) Pitted terrain on Vesta and implications for the presence of volatiles. *Science* **338**, 246–249.

Dohmen R., Chakraborty S., Palme H. and Rammensee W. (1998) Solid-solid reactions mediated by a gas phase: An experimental study of reaction progress and the role of surfaces in the system olivine iron metal. *Am. Mineral.* **83**, 970–984.

Duke M. B. and Silver L. T. (1967) Petrology of eucrites, howardites and mesosiderites. *Geochim. Cosmochim. Acta* **31**, 1637-1665.

Gounelle M., Zolensky M. E., Liou J. C., Bland P. A., and Alard O. (2003) Mineralogy of carbonaceous chondritic microclasts in howardites: Identification of C2 fossil micrometeorites. *Geochim. Cosmochim. Acta* **67**, 507-527.

Harlow G. E. and Klimentidis R. (1980) Clouding of pyroxene and plagioclase in eucrites – implications for post-crystallization processing. *Proc. Lunar Planet. Sci. Conf.* **11**, 1131–1143.

Janots E., Gnos E., Hofmann B. A., Greenwood R. C., Franchi I. A., Bermingham K., and Netwing V. (2012) Jiddat al Harasis 556: A howardite impact melt breccia with an H chondrite component. *Meteor. Planet. Sci* **47**, 1558-1574.

Kennedy T., Jourdan F., Eroglu E., and Mayers C. (2019) Bombardment history of asteroid 4 Vesta recorded by brecciated eucrites: Large impact event clusters at 4.50 Ga and discreet bombardment until 3.47 Ga. *Geochim. Cosmochim. Acta* **260**, 99-123.

Kurat G., Varela M. E., Zinner E., Maruoka T. and Brandstätter F. (2003) Major, minor and trace elements in some glasses from the NWA 1664 howardite. *Lunar Planet. Sci. Conf.* **34**, #1733 (abstract).

Lorenz K. A., Nazarov M. A., Kurat G., Brandstätter F., and Ntaflos T. (2007) Foreign meteoritic material of howardites and polymict eucrites. *Petrology* **15**, 109-125.

Mayne R. G., Smith S. E., and Corrigan C. M. (2016) Hiding in the howardites: Unequilibrated eucrite clasts as a guide to the formation of Vesta's crust. *Meteor. Planet. Sci.* **51**, 2387-2402.

McCord T. B., Li J. Y., Combe J. P., McSween H. Y., Jaumann R., Reddy V., Tosi F., Williams D., Blewett D. T., Turrini N. D., Palomba E., Pieters C. M., De Sanctis M. C., Ammannito E., Capria M. T., Le Corre L., Longobardo A., Nathues A., Mittlefehldt D. W., Schroder S. E., Hiesinger H., Beck A. W., Capaccioni F., Carsenty U., Keller H. U., Denevi B. W., Sunshine J. M., Raymond C. A., and Russell C. T. (2012) Dark material on Vesta from the infall of carbonaceous volatile-rich material. *Nature* **491**, 83–86..

McSween H. Y., Binzel R. P., De Sanctis M. C., Ammannito E., Prettyman T. H., Beck A. W., Reddy V., Le Corre L., Gaffey M. J., McCord T. B., Raymond C. A., Russell C. T. and the Dawn mission team (2013) Dawn; the Vesta-HED connection; and the geologic context for eucrites, diogenites, and howardites. *Meteor. Planet. Sci.* **48**, 2090–2104.

Metzler K., Bobe K. D., Palme H., Spettel B., and Stöffler D. (1995) Thermal and impact metamorphism on the HED parent asteroid. *Planet. Space Sci.* **43**: 499-525.

Mittlefehldt D. W. and Lindstrom M. M. (1997) Magnesian basalt clasts from the EET 92014 and Kapoeta howardites and a discussion of alleged primary magnesian HED basalts. *Geochim. Cosmochim. Acta* **61**, 453-462.

Mittlefehldt D. W. (2015) Asteroid (4) Vesta: I. The howardite-eucrite-diogenite (HED) clan of meteorites. *Geochemistry* **75**, 155-183.

Nathues A., Hoffmann M., Cloutis E. A., Schäfer M., Reddy V., Christensen U., Sierks H., Thangjam G. S., Le Corre L., Mengel K., Vincent J. B., Russell C. T., Prettyman T., Schmedemann N., Kneissl T., Raymond C., Gutierrez-Marques P., Büttner I., and Hall I. (2014) Detection of serpentine in exogenic carbonaceous chondrite material on Vesta from Dawn FC data. *Icarus* **239**, 222–237.

Pang R. L., Zhang A. C., and Wang R. C. (2017) Complex origins of silicate veinlets in HED meteorites: A case study of Northwest Africa 1109. *Meteor. Planet. Sci*. **52**, 2113-2131.

Papike J. J. (1998) Comparative planetary mineralogy: chemistry of melt-derived pyroxene, feldspar, and olivine. *In Planetary Materials* (ed. J. J. Papike). Rev. Mineral. **36**, 7-01–7-11

Patzer A. and McSween Jr H. Y. (2012) Ordinary (mesostasis) and not- so- ordinary (symplectites) late- stage assemblages in howardites. *Meteor. Planet. Sci*. **47**, 1475-1490.

Patzer A. and McSween Jr H. Y. (2018) Ferroan olivine- bearing eucrite clasts found in howardites. *Meteor. Planet. Sci*. **53**, 1131-1149.

Prettyman T. H., Mittlefehldt D. W., Yamashita N., Lawrence D. J., Beck A. W., Feldman W. C., McCoy T. J., McSween H. Y., Toplis M. J., Titus T. N., Tricarico P., Reedy R. C., Hendricks J. S., Forni O., Le Corre L., Li J.-Y., Mizzon H., Reddy V., Raymond C. A., and Russell C. T. (2012) Elemental mapping by Dawn reveals exogenic H in Vesta's regolith. *Science* **338**, 242–246.

Reddy V., Le Corre L., O'Brien D. P., Nathues A., Cloutis E. A., Durda D. D., Bottke W. F., Bhatt M. U., Nesvorný D., Buczkowski D., Scully J. E. C., Palmer E. M., Sierks H., Mann P. J., Becker K. J., Beck A. W., Mittlefehldt D., Li J.-Y., Gaskell R., Russell C. T., Gaffey M. J., McSween H. Y., McCord T. B., Combe J.-P., and Blewett D. (2012) Delivery of dark material to Vesta via carbonaceous chondritic impacts. *Icarus* **221**, 544–559, Rombeck S., Vollmer C., Roszjar J., Sarafian A. R., and Klemme S. (2021) How do secondary iron enrichments form within basaltic eucrites? An experimental approach. *Meteor. Planet. Sci*. **56,** 911-928.

Roszjar J., Metzler K., Bischoff A., Barrat J., Geisler T., Greenwood R. C., Franchi I. A. and Klemme S. (2011) Thermal history of Northwest Africa (NWA) 5073 – a coarse grained Stannern-trend eucrite containing cm-sized pyroxenes and large zircon grains. *Meteor. Planet. Sci.* **46**, 1754–1773.

Russell C. T., Raymond C. A., Jaumann R., McSween H. Y., De Sanctis M. C., Nathues A., Prettyman T. H., Ammannito E., Reddy V. and Preusker F., et al. (2013) Dawn completes its mission at 4 Vesta. *Meteor. Planet. Sci.* **48**, 2076–2089.

Ruzicka A., Grossman J., Bouvier A., and Agee C. B. (2017) The meteoritical bulletin, No. 103. *Meteor. Planet. Sci.* **52**, 1014.

Sanctis M. C. D., Combe J. P., Ammannito E., Palomba E., Longobardo A., McCord T. B., Marchi S., Capaccioni F., Capria M. T. and Mittlefehldt D. W., et al. (2012) Detection of widespread hydrated materials on Vesta by the VIR imaging spectrometer on board the Dawn Mission. *Astrophys. J.* **758**, L36.

Sanctis M. C. D., Ammannito E., Capria M. T., Capaccioni F., Combe J. P., Frigeri A., Longobardo A., Magni G., Marchi S., McCord T. B., Palomba E., Tosi F., Zambon F., Carraro F., Fonte S., Li Y. J., McFadden L. A., Mittlefehldt D. W., Pieters C. M., Jaumann R., Stephan K., Raymond C. A., and Russell C. T. (2013) Vesta's mineralogical composition as revealed by the visible and infrared spectrometer on dawn. *Meteorit. Planet. Sci.* **48**, 2166-2184

Sarafian A. R., Roden M. F., and Patiño- Douce A. E. (2013) The volatile content of Vesta: Clues from apatite in eucrites. *Meteor. Planet. Sci*. **48**, 2135-2154.

Sarafian A. R., John T., Roszjar J., and Whitehouse M. J. (2017) Chlorine and hydrogen degassing in Vesta's magma ocean. *Earth and Planet. Sci. Lett.* **459**, 311-319.

Schwartz J. M. and McCallum I. S. (2005) Comparative study of equilibrated and unequilibrated eucrites: subsolidus thermal histories of Haraiya and Pasamonte. *Am. Mineral.* **90**, 1871–1886.

Scully J. E., Russell C. T, Yin A., Jaumann R., Carey E., Castillo-Rogez J., McSween H. Y., Raymond C. A., Reddy V., Le Corre L. (2015) Geomorphological evidence for transient water flow on Vesta. *Earth Planet. Sci. Lett.* **411**, 151-163.

Shirai N., Okamoto C., Yamaguchi A., and Ebihara M. (2016) Siderophile elements in brecciated HED meteorites and the nature of projectile materials in HED meteorites. *Earth Planet. Sci. Lett.* **437**, 57-65.

Stolper, E. (1977) Experimental petrology of eucritic meteorites. *Geochim. Cosmochim. Acta* **41**, 587-611.

Takeda H., Wooden J. L., Mori H., Delaney J. S., Prinz M. and Nyquist L. E. (1983) Comparison of Yamato and Victoria Land polymict eucrites: a view from mineralogical and isotopic studies. *Proc. 14th Lunar Planet. Sci. Conf., J. Geophys. Res.* **88**, B245–B256

Takeda H. and Graham A. L. (1991) Degree of equilibration of eucritic pyroxenes and thermal metamorphism of the earliest planetary crust. *Meteoritics* **26**, 129–134

Takeda H., Mori H. and Bogard D. D. (1994) Mineralogy and ^{39}Ar-^{40}Ar age of an old pristine basalt: thermal history of the HED parent body. *Earth Planet. Sci. Lett.* **122**, 183–194.

Treiman A. H., Lanzirotti A. and Xirouchakis D. (2004) Ancient water on asteroid 4-Vesta: evidence from a quartz veinlet in the Serra de Magé eucrite meteorite. *Earth Planet. Sci. Lett.* **219**, 189–199.

Unsalan O., Jenniskens P., Qing- Zhu Y., Kaygisiz E., Albers J., Clark D. L., Granvik M. et al. (2019) The Sariçiçek howardite fall in Turkey: Source crater of HED meteorites on Vesta and impact risk of Vestoids. *Meteorit. Planet. Sci.* **54**, 953-1008.

Vaci Z., Day J., Paquet M., Ziegler K., Yin Q.Z., Dey S., Miller A., Agee C. B., Bartoschewitz R. and Pack A. (2021) Olivine-rich achondrites from Vesta and the missing mantle problem. *Nature communications* **12**, 1-8.

Vollmer C., Rombeck S., Roszjar J., Sarafian A. R., and Klemme S. (2020) The brecciated texture of polymict eucrites: Petrographic investigations of unequilibrated meteorites from the Antarctic Yamato collection. *Meteor. Planet. Sci*. **55**, 558-574.

Warren P. H. (2002) Northwest Africa 1000: A New eucrite with maskelynite, unequilibrated pyroxene crisscrossed by fayalite-rich veins and Stannern-like geochemistry. *Lunar Planet. Sci. Conf.* **33**, #1147 (abstract).

Warren P. H., Rubin A. E., Isa J., Gessler N., Ahn I., and Choi B. G. (2014) Northwest Africa 5738: Multistage fluid-driven secondary alteration in an extraordinarily evolved eucrite. *Geochim. Cosmochim. Acta* **141**, 199-227.

Warren P. H., Isa J., Ebihara M., Yamaguchi A., and Baecker B. (2017) Secondary‐ volatiles linked metallic iron in eucrites: The dual‐ origin metals of Camel Donga. *Meteor. Planet. Sci*. **52**, 737-761.

Warren P. H., Esposito R., and Manning C. (2018) Secondary, aqueous (?), metasomatic olivine veins in Apollo 14 mare basalt 1472 (abstract #2747). *Lunar Planet. Sci. Conf.* **49**, #2747 (abstract).

Wlotzka F. (2005) Cr spinel and chromite as petrogenetic indicators in ordinary chondrites: Equilibration temperatures of petrologic types 3.7 to 6. *Meteor. Planet. Sci*. **40**, 1673-1702.

Yamaguchi A., Taylor G. J. and Keil K. (1996) Global crustal metamorphism of the eucrite parent body. *Icarus* **124**, 97–112.

Yamaguchi A., Taylor G. J., and Keil K. (1997) Metamorphic history of the eucritic crust of 4 Vesta. *J. Geoph. Res.: Planets* **102**, 13381-13386.

Yamaguchi A. (2000) Spinels in basaltic eucrites: implication for crystallization and metamorphic history (abstract). *Meteor. Planet. Sci.* **35**, A174.

Yamaguchi A. and Mikouchi T. (2005) Heating Experiments of the HaH 262 Eucrite and Implication for the Metamorphic History of Highly Metamorphosed Eucrites. *Lunar Planet. Sci. Conf.* **36**, #1574 (abstract).

Yamaguchi A., Mikouchi T., Ito M., Shirai N., Barrat J. A., Messenger S., and Ebihara M. (2013) Experimental evidence of fast transport of trace elements in planetary basaltic crusts by high temperature metamorphism. *Earth Planet. Sci. Lett.* **368**, 101-109.

Yesiltas M., Glotch T. D., Jaret S., Verchovsky A. B., and Greenwood R. C. (2019) Carbonaceous matter in the Sariçiçek meteorite. *Meteor. Planet. Sci*. **54**, 1495-1511.

Zeng X., Li S., Joy K. H., Li X., Liu J., Li Y., Li R., and Wang S. (2020) Occurrence and implications of secondary olivine veinlets in lunar highland breccia Northwest Africa 11273. *Meteor. Planet. Sci*. **55**, 36–55.

Zhang A. C., Wang R. C., Hsu W. B., and Bartoschewitz R. (2013) Record of S-rich vapors on asteroid 4 Vesta: Sulfurization in the Northwest Africa 2339 eucrite. *Geochim. Cosmochim. Acta* **109**, 1–13.

Zhang A. C., Bu Y. F., Pang R. L., Sakamoto N., Yurimoto H., Chen L. H., Gao J. F., Du D. H., Wang X. L., and Wang R. C. (2018) Origin and implications of troilite-orthopyroxene intergrowths in the brecciated diogenite Northwest Africa 7183. *Geochim. Cosmochim. Acta* **220**, 125–145.

Zhang A. C., Kawasaki N., Bao H., Liu J., Qin L., Kuroda M., Gao J. F., Chen L. H., He Y., Sakamoto N., and Yurimoto H. (2020) Evidence of metasomatism in the interior of Vesta. *Nature Communications* **11**, 1289–1296.

Zolensky M. E., Weisberg M. K., Buchanan P. C., and Mittlefehldt D. W. (1996) Mineralogy of carbonaceous chondrite clasts in HED achondrites and the Moon. *Meteor. Planet. Sci*. **31**, 518-537.

TABLES

Table 1

Average EPMA analysis (wt%) of pyroxene, olivine in veinlets, primary and secondary plagioclase in NWA 11911 (Stdev=Standard deviation)

NWA 11911	n	SiO_2	TiO_2	Al_2O_3	Cr_2O_3	FeO	MnO	MgO	CaO	Na_2O	K_2O	P_2O_5	Total	Fs/Fa/An	En/Fo/Ab	Wo/La/Or
Fe-enriched px (Fig. **1**)																
Dark cores	9	52.04	0.17	1.28	0.70	22.25	0.74	19.77	3.26	0.01	0	0.01	100.27	36.11	57.12	6.78
Stdev		0.77	0.05	0.25	0.15	1.52	0.06	1.57	0.57	0.01	0	0.01	0.55	2.82	3.97	1.26
Fe-enriched pyroxene	7	49.96	0.21	0.90	0.37	31.94	0.94	13.02	2.81	0.01	0	0.01	100.23	54.35	39.51	6.14
Stdev		0.57	0.12	0.15	0.14	1.94	0.06	0.91	1.56	0.01	0	0.03	0.46	3.10	2.70	3.43
Fe-enriched px (Fig. **1**)																
Mg-rich core	3	51.12	0.33	0.64	0.42	27.35	0.85	16.98	2.53	n.d.	0	0.01	100.27	44.95	49.73	5.32
Stdev		0.33	0.10	0.38	0.45	1.12	0.04	0.54	0.39	-	0	0.01	0.18	2.02	1.33	0.80
Fe-enriched px	3	50.36	0.31	0.70	0.23	31.65	0.95	13.67	2.39	0.01	0	0.01	100.32	53.57	41.24	5.18
Stdev		0.17	0.07	0.42	0.15	1.29	0.05	0.43	0.89	0.01	0.01	0.02	0.10	1.90	1.34	1.96
Remnant Ca-zoning (Fragment in Fig. **1**e)	1	49.87	0.43	1.23	0.55	16.67	0.49	11.23	18.52	0.03	0	0	100.10	50.10	39.64	10.27
Ca-rich exsolution lamellae (Equilibrated fragment in Fig. **1**f)	1	49.97	1.14	1.53	0.55	16.67	0.49	11.23	18.52	0.03	0	0	100.19	27.60	33.12	39.28
Plagioclase-silica assemblage	2	78.77	0.16	12.49	0.02	1.40	0.06	0.39	6.34	0.47	0.09	0.09	100.31			
Stdev		6.04	0.06	3.40	-	0.68	0.03	0.22	1.73	0.08	0.01	0.05	0.24			
Olivine-bearing unequilibrated fragments																
(Fig. **2**, Fig. **S**4)																
Mg-core	17	51.78	0.13	1.20	0.66	22.21	0.75	20.49	2.92	0.02	0	0.02	100.21	35.55	58.46	5.99
Stdev		0.60	0.03	0.09	0.05	0.68	0.05	0.73	0.27	0.02	0.01	0.01	0.43	1.27	1.62	0.60
Fe-enriched pyroxene	19	49.32	0.14	0.82	0.47	32.98	1.00	13.38	2.24	0.01	0	0.01	100.45	55.25	39.95	4.80
Stdev		1.04	0.04	0.41	0.23	1.24	0.06	0.58	0.49	0.01	0.01	0.02	0.83	1.83	1.49	1.06
Olivine veinlets	12	31.92	0.04	0.29	0.37	56.71	1.27	9.29	0.46	0.02	0	0.03	100.45	76.79	22.42	0.79
Stdev		1.74	0.04	0.45	0.82	1.74	0.08	0.85	0.59	0.04	0.01	0.04	1.31	2.38	2.03	1.00
Secondary plagioclase	3	41.90	0.00	34.33	0.01	1.20	0.04	0.22	20.16	0.28	0.03	0.25	98.61	97.40	2.44	0.16

Stdev		2.01	0.01	1.39	0.01	0.11	0.01	0.17	1.93	0.08	0.01	0.17	1.90	0.86	0.80	0.09
Primary plagioclase	17	44.83	0.013	35.20	0.005	0.310	0.014	0.15	18.3	1.070	0.053	0.066	100.04	90.134	9.552	0.31
Stdev		0.829	0.010	1.332	0.014	0.259	0.013	0.22	0.63	0.247	0.022	0.092	1.444	2.380	2.28	0.13
Ca-rich pyroxene areas	6	47.07	0.08	0.39	0.11	32.15	0.92	11.35	7.735	0.021	0.005	0.057	100	51.52	32.71	15.76
Stdev		3.88	0.032	0.073	0.058	3.823	0.083	1.621	2.544	0.023	0.009	0.059	1.124	4.575	5.99	4.52
Olivine-bearing equilibrated fragments (Fig. 7)																
Host pyroxene	5	48.33	0.39	0.82	0.51	32.81	1.02	11.26	5.07	0.01	0	0.03	100.26	55.27	33.80	10.93
Stdev		0.55	0.05	0.14	0.48	1.25	0.06	0.40	0.80	0	0.01	0.03	0.84	2.18	1.03	1.70
Olivine veinlets	9	32.63	0.08	0.16	0.09	56.27	1.28	7.94	1.42	0.02	0.01	0.03	100.09	77.87	19.60	2.54
Stdev		2.00	0.06	0.13	0.13	2.97	0.18	0.81	1.25	0.02	0.01	0.02	1.23	3.17	1.88	2.26
Plagioclase	6	44.97	0.03	32.10	0.01	1.73	0.06	0.42	17.14	0.86	0.09	0.09	97.58	91.32	8.08	0.60
Stdev		1.28	0.04	2.31	0.01	1.70	0.05	0.43	0.91	0.35	0.06	0.06	2.35	2.70	2.99	0.47

Table 2

Average EPMA analysis (wt%) of metasomatized pyroxene, olivine in veinlets, primary and secondary plagioclase in NWA 1664 and NWA 8675 (n.a. = not analyzed; n.d. = not detected; Stdev= Standard deviation)

NWA 1664	n	SiO_2	TiO_2	Al_2O_3	Cr_2O_3	FeO	MnO	MgO	CaO	Na_2O	K_2O	P_2O_5	Total	Fs/Fa/An	En/Fo/Ab	Wo/La/Or
Mg-cores	122	51.37	0.12	1.17	0.98	20.83	0.65	22.32	1.86	0.01	0.01	n.a.	99.32	33.18	63.03	3.79
Stdev		1.06	0.03	0.16	0.48	3.79	0.09	2.75	0.51	0.02	0.01	n.a.	0.46	6.7	6.66	1.04
Fe-enriched px	10	48.2	0.15	0.37	0.77	31.94	0.96	16.39	1.02	0.01	0	n.a.	99.83	50.99	46.87	2.13
Stdev		2.5	0.06	0.24	0.89	3.68	0.04	0.28	0.4	0.01	0	n.a.	0.36	3.21	2.5	0.87
Olivine veinlets	27	32.26	0.03	0.03	0.06	51.17	1.07	15.05	0.11	0.01	0	n.a.	99.8	65.48	34.34	0.18
Stdev		0.73	0.07	0.03	0.05	1.14	0.06	0.38	0.08	0.02	0.01	n.a.	0.74	1.08	1	0.14
Secondary plagioclase	4	42.62	0.03	35.83	0.01	1.25	0.01	0.23	20.02	0.22	0.02	n.a.	100.23	97.96	1.92	0.11

Stdev		0.23	0.02	0.59	0.02	0.14	0.01	0.22	0.3	0.03	0.01	n.a.	0.6	0.29	0.27	0.03
Primary plagioclase	5	46.78	0.04	32.86	0	0.53	0.01	0.12	17.24	1.64	0.06	n.a.	99.29	84.95	14.67	0.37
Stdev		1.1	0.02	0.91	0	0.41	0.03	0.21	0.67	0.3	0.03	n.a.	0.65	2.86	2.7	0.19
NWA 8675																
Mg-cores	28	52.57	0.19	1.09	0.61	22.31	0.74	20.27	3.33	0.02	0	0.01	101.17	35.62	57.58	6.8
Stdev		0.66	0.05	0.27	0.21	1.8	0.04	1.34	0.42	0.02	0	0.01	0.28	3.31	3.26	0.85
Fe-enriched px	40	49.52	0.21	0.91	0.45	33.54	0.94	12.28	3.35	0.01	0	0.02	101.26	56.13	36.67	7.2
Stdev		1.25	0.09	0.38	0.31	2.73	0.1	1.1	1.17	0.01	0.01	0.02	0.45	3.77	3.33	2.53
High-Ca px	7	49.33	0.81	0.84	0.35	26.54	0.82	9.81	12.37	0.01	0.01	0.01	100.94	44.35	29.2	26.45
Stdev		0.42	0.39	0.44	0.18	2.34	0.1	0.18	2.24	0.01	0.01	0.02	0.38	4.14	0.6	4.66
Olivine veinlets	13	31.4	0.03	0.08	0.01	59.17	1.29	7.92	0.24	0.01	0	0.03	100.21	80.38	19.2	0.43
Stdev		1.41	0.03	0.18	0.01	1.18	0.05	0.31	0.13	0.02	0.01	0.03	1.22	0.97	0.86	0.23
Secondary plagioclase	2	43.41	0.01	35.73	0	1.46	0.06	0.13	20.16	0.23	0	0.05	101.23	98	2	0
Stdev		0.03	0.01	0.25	0	0.07	0.01	0	0.15	0.03	0	0.02	0.32	0.3	0.3	0
Primary plagioclase	27	47.16	0.04	33.65	0	0.42	0.02	0.08	17.76	1.41	0.11	0.03	100.7	86.88	12.48	0.64
Stdev		0.46	0.04	0.66	0	0.55	0.05	0.19	0.35	0.12	0.03	0.02	0.41	1.15	1.04	0.21
NWA 13269																
Pyroxene host (phenocrysts)	15	50.31	0.23	0.57	0.90	29.88	0.95	15.25	1.08	0.00	0.01	n.d.	99.20	51.13	46.49	2.37
Stdev		0.98	0.12	0.53	0.88	0.88	0.04	0.76	0.33	0.01	0.01	-	0.48	1.66	1.91	0.73
Low-Ca px (groundmass)	3	49.60	0.37	0.38	1.28	28.79	0.92	13.32	5.39	0.02	n.d.	n.d.	100.12	48.50	39.94	11.56
Stdev		1.51	0.16	0.01	0.95	2.68	0.09	0.42	2.90	0.01	-	-	0.66	5.22	1.18	6.04
High-Ca px	9	52.02	0.31	0.56	0.19	16.39	0.58	12.33	17.61	0.03	0.01	0.01	100.10	27.02	36.10	36.88
Stdev		0.66	0.13	0.16	0.04	4.56	0.15	0.49	4.92	0.02	0.01	0.01	0.52	8.03	1.90	9.83
Primary plagioclase	13	47.33	0.02	32.97	0.01	0.40	0.01	0.03	16.32	1.64	0.35	0.03	99.11	82.81	15.05	2.14
Stdev		1.29	0.01	0.95	0.01	0.22	0.01	0.02	0.84	0.32	0.40	0.03	0.83	3.27	2.83	2.51
Secondary plagioclase	2	42.85	0.01	35.77	0.01	0.84	0.03	0.03	19.25	0.30	0.01	0.03	99.16	97.25	2.70	0.04

Stdev	0.19	0.02	0.19	0.01	0.06	0.00	0.02	0.09	0.02	0.01	0.04	0.51	0.10	0.16	0.06

Table. 3

Average EPMA analysis (wt%) of primary and secondary Cr-spinel associated with olivine veinlets in NWA 11911 and NWA 1664 (n.d. = not detected; Stdev= Standard deviation)

	n	SiO_2	TiO_2	Al_2O_3	Cr_2O_3	FeO	MnO	MgO	CaO	Na_2O	K_2O	Total	Ulv	Spl	Chr	Fe^{3+}/Fe^{2+}	T(°C) *
NWA 11911																	
Secondary Cr-spinel	4	0.11	2.54	9.46	49.86	35.55	0.21	0.41	0.42	0.01	0	98.99	6.9	20.12	71.16	0.03	753.79
Stdev		0.08	0.4	0.23	0.87	0.68	0.24	0.01	0.09	0.01	0	0.6	1.07	0.36	1.24	0.01	9.78
Primary Cr-spinel	3	5.48	2.1	8.2	41.52	35.17	0.51	1.95	1.63	0.02	0.02	97.22	5.85	17.73	60.41	-	-
Stdev		7.92	0.8	1.52	10.84	4	0.14	2.32	1.16	0.03	0.01	1.52	2.48	3.87	17.97	-	
NWA 1664																	
Secondary Cr-spinel	8	3.47	2.41	10.67	42.52	35.97	0.52	1.75	0.39	0.01	0	98.27	6.46	22.31	59.67	0.02	762.8
Stdev		2.97	0.97	1.13	2.96	1.39	0.05	0.99	0.85	0.01	0	1.2	2.7	2.52	4.86	0.02	89.36
NWA 13269																	
Secondary Cr-spinel	3	0.14	2.59	10.73	47.52	34.27	0.63	1.04	0.09	0.00	n.d.	97.09	7.03	22.83	67.87	0.04	-
Stdev		0.13	0.58	1.38	0.87	0.34	0.03	0.19	0.05	0.01	0.00	0.79	1.58	2.73	1.70	0.02	-

*Equilibration temperatures calculated using chromite and olivine compositions (Mg and Fe apfu in olivine and Al, Cr, Mg and Fe apfu in chromite) based on the method of Wlotzka (2005).

FIGURES

3. RESULTS

3.2. FE-ENRICHMENT IN PYROXENE

Unequilibrated pyroxene fragments

Unequilibrated basaltic clasts

Slightly equilibrated pyroxene fragments

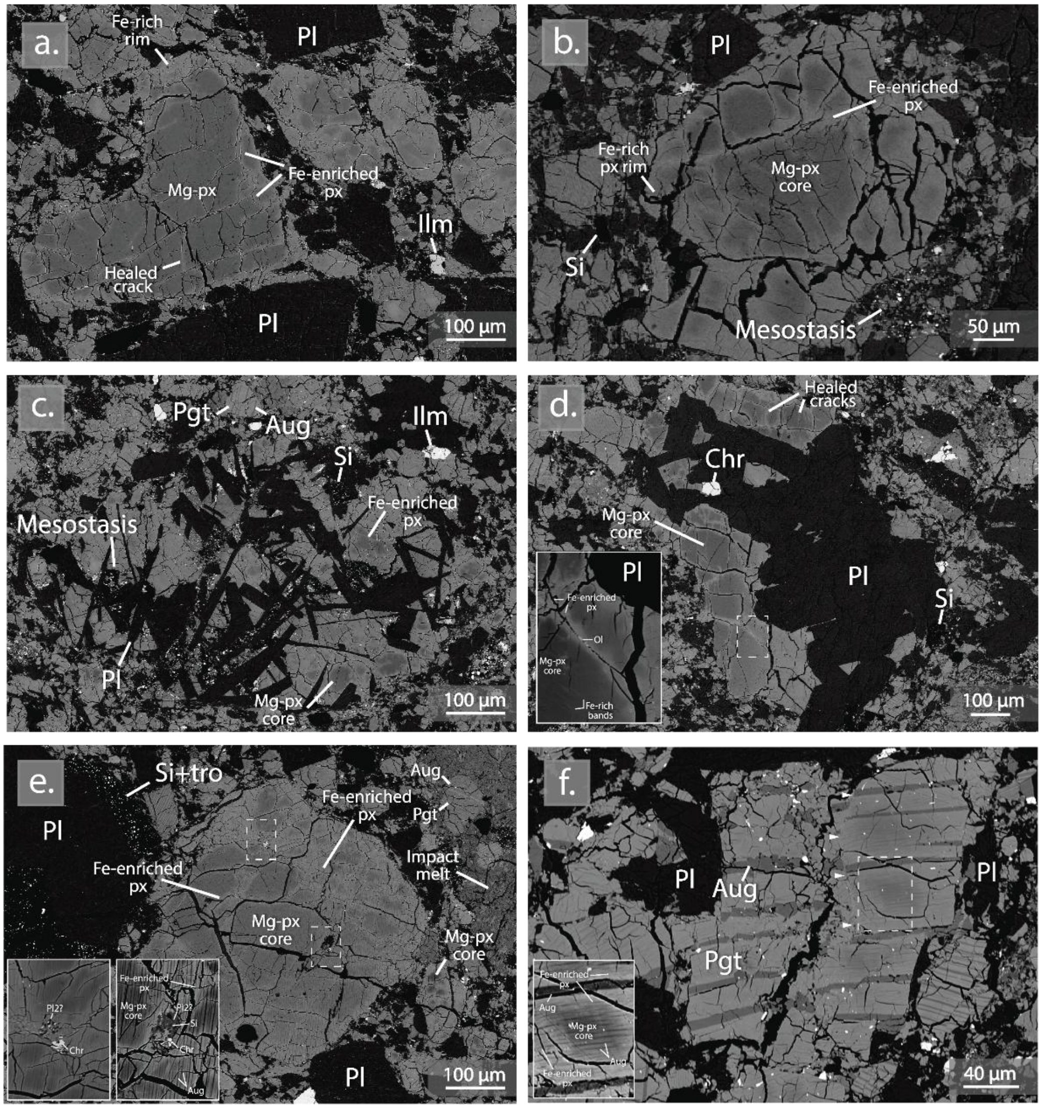

Fig. 1. Back-scattered electron images of pyroxene fragments and clasts displaying Fe-enrichment along cracks in NWA 11911. (a, b) Unequilibrated, Fe-enriched pyroxene fragments. (c) Subophitic clast containing Fe-enriched pyroxene. Note that Fe-enrichment in pyroxene is located mainly in the lower part of the clast. Bright Fe-rich bands are crossing Mg-cores. (d) Subophitic clast dominated by coarse plagioclase and zoned pyroxene. Chromite is also present. Frequent deposition of bright phases in cracks is observed. (e, f) Slightly equilibrated and fractured pyroxenes displaying Fe-enrichment in cracks. Pgt = pigeonite; Aug = augite; Px = pyroxene; Pl = plagioclase; Si= Silica; Ilm = ilmenite; Tro = troilite; Chr = chromite; Pl2 = secondary plagioclase.

3.2. FAYALATIC VEINLETS AND ASSOCIATED PHASES

Unequilibrated pyroxene fragments and clasts

NWA 11911

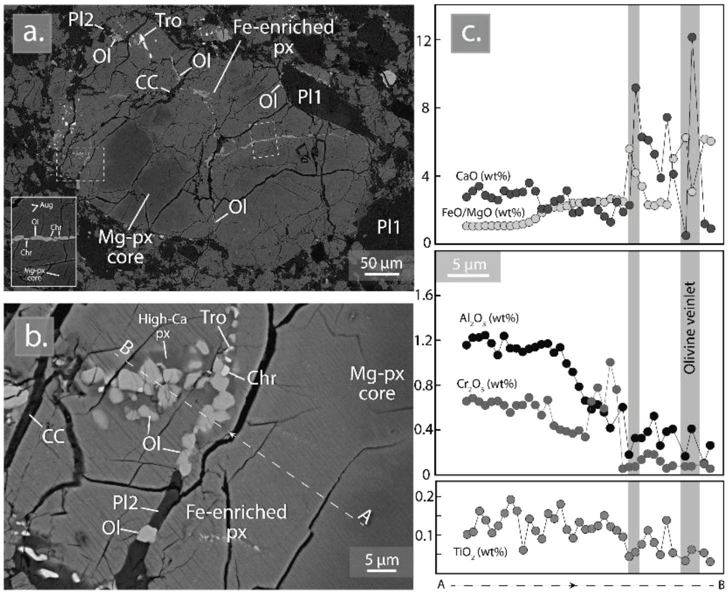

Fig. 2. SEM images of secondary olivine veinlets associated with Ca-rich plagioclase, Cr-spinel and troilite in NWA 11911. Ol = olivine; Px = pyroxene; Aug = augite; Pl1 = primary plagioclase; Pl2 = secondary plagioclase; Chr = chromite; Tro = troilite, CC = calcite (terrestrial weathering product).

NWA 1664

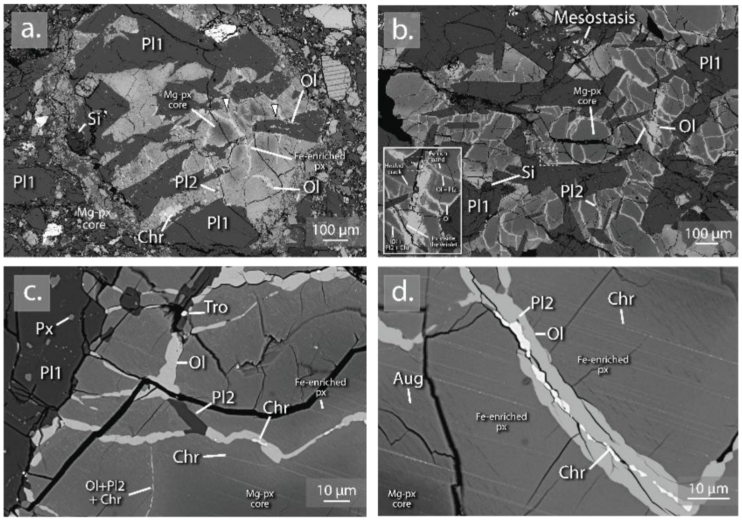

Fig. 3. BSE images of the olivine veinlets found in NWA 1664. Dashed squares (b) show plagioclase penetrated or crossed by the veinlets. Note the lack of augite exsolution lamellae near the veinlets in (c) and (d). Healing of pyroxene, resulting in the discontinuity of the veinlet, is observed in the upper left area in (d). Ol = olivine; Px =

pyroxene; Aug = augite; Pl1 = primary plagioclase; Pl2 = secondary plagioclase; Si = silica; Chr = chromite; Tro = troilite.

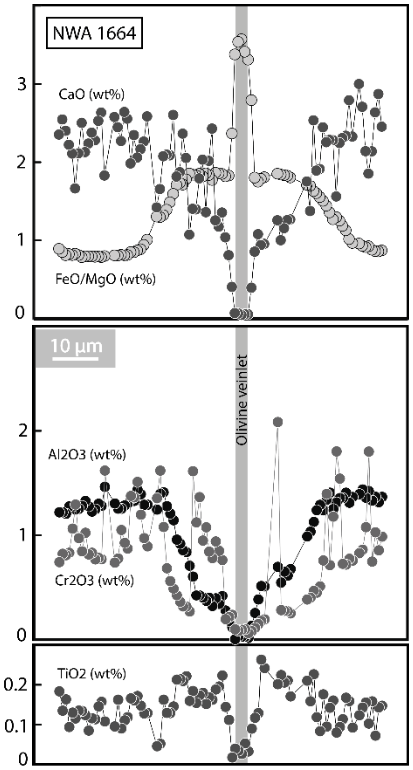

Fig. 4. EPMA profile across pristine pyroxene, Fe-enriched pyroxene and an olivine veinlet in NWA 1664.

NWA 8675

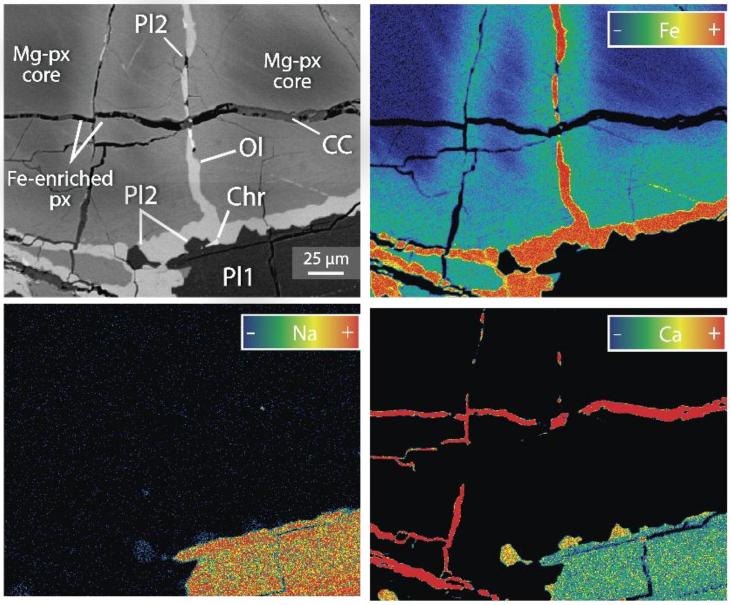

Fig. 5. SEM and EPMA-WDS maps of Fe-enriched pyroxene and olivine veinlets associated with secondary plagioclase and Cr-spinel in NWA 8675. Note the parallel Fe-rich bands penetrating the Mg-cores. The Ca-rich veins shown in the Ca map are fractures filled with calcite (terrestrial weathering product). Ol = olivine; Px = pyroxene; Pl1 = primary plagioclase; Pl2 = secondary plagioclase; Chr = chromite; CC = calcite.

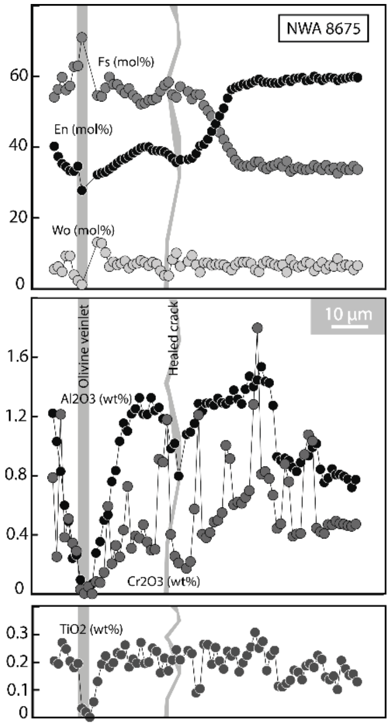

Fig. 6. EPMA profile across Fe-enriched pyroxene, a healed crack, a fayalitic veinlet and a Mg-core in NWA 8675.

Equilibrated pyroxene fragments

NWA 11911

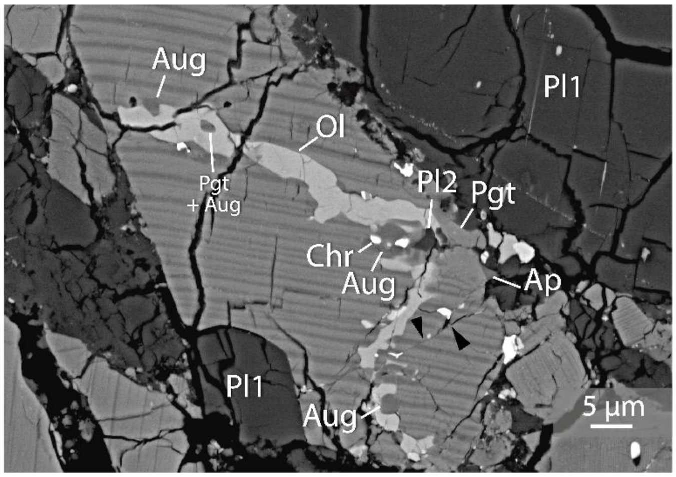

Fig. 7. Olivine veinlet crossing pyroxene exhibiting exsolution of high-Ca lamellae in NWA 11911. Note the presence of exsolved pyroxene fragment within the veinlet. Associated secondary phases are chromite and likely plagioclase. Ca-rich and low-Ca areas are observed within or in vicinity of the veinlet. The pyroxene host is faulted as indicated by the black triangle arrows. Ca-Px = High-Ca pyroxene; Low-Ca Px = Low-Ca pyroxene; Pl1= Primary plagioclase; Pl2 = Secondary plagioclase; Ol = Olivine; Cr = Chromite; Fe= Fe metal; Ap = Apatite.

3.3. SECONDARY PLAGIOCLASE VEINLETS

NWA 13269

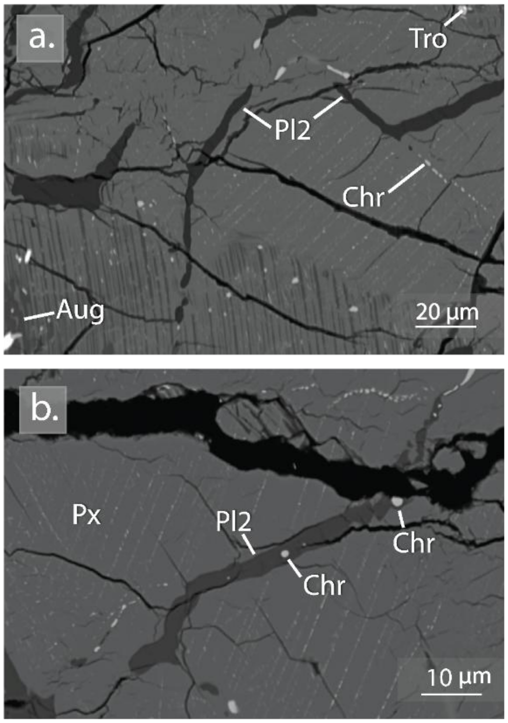

Fig. 8. SEM images of Ca-rich plagioclase veinlets in the unbrecciated basaltic eucrite NWA 13269. These veinlets are filling cracks in both pyroxene phenocrysts (containing Cr-rich, bright lamellae) and pyroxene within the groundmass (containing Ca-rich exsolution lamellae). Note the abrupt change of the direction of the veinlet when crossing the grain boundaries. Px = pyroxene; Pl2 = secondary plagioclase; Chr = chromite; Tro = troilite.

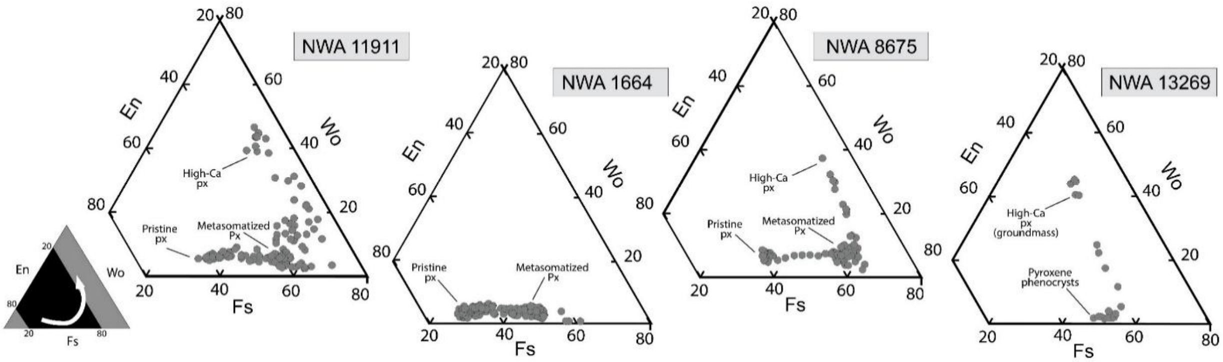

Fig. 9. Pyroxene end-member composition in NWA 11911, NWA 1664, NWA 8675 and NWA 13269. Most of pyroxenes follow a Mg-Fe-Ca trend, as indicated by the white arrow in the grey triangle illustrated on the left.

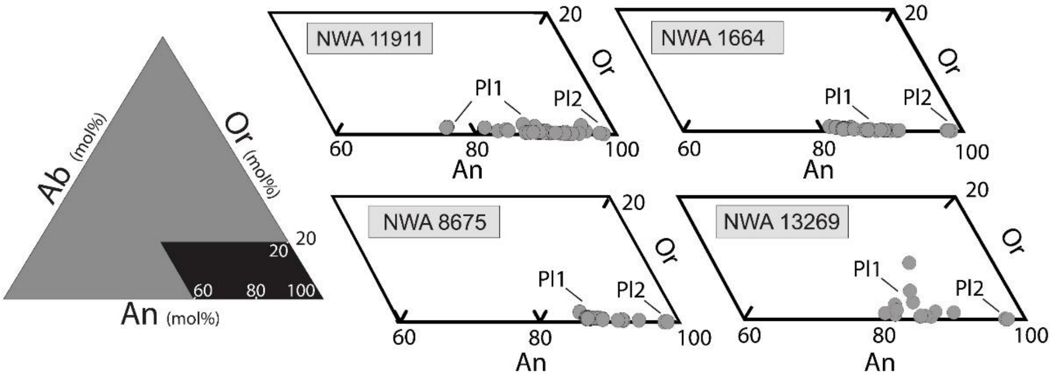

Fig. 10. Primary and secondary plagioclase compositions in NWA 11911, NWA 1664, NWA 8675 and NWA 13269. Pl1 = primary plagioclase; Pl2 = secondary plagioclase.

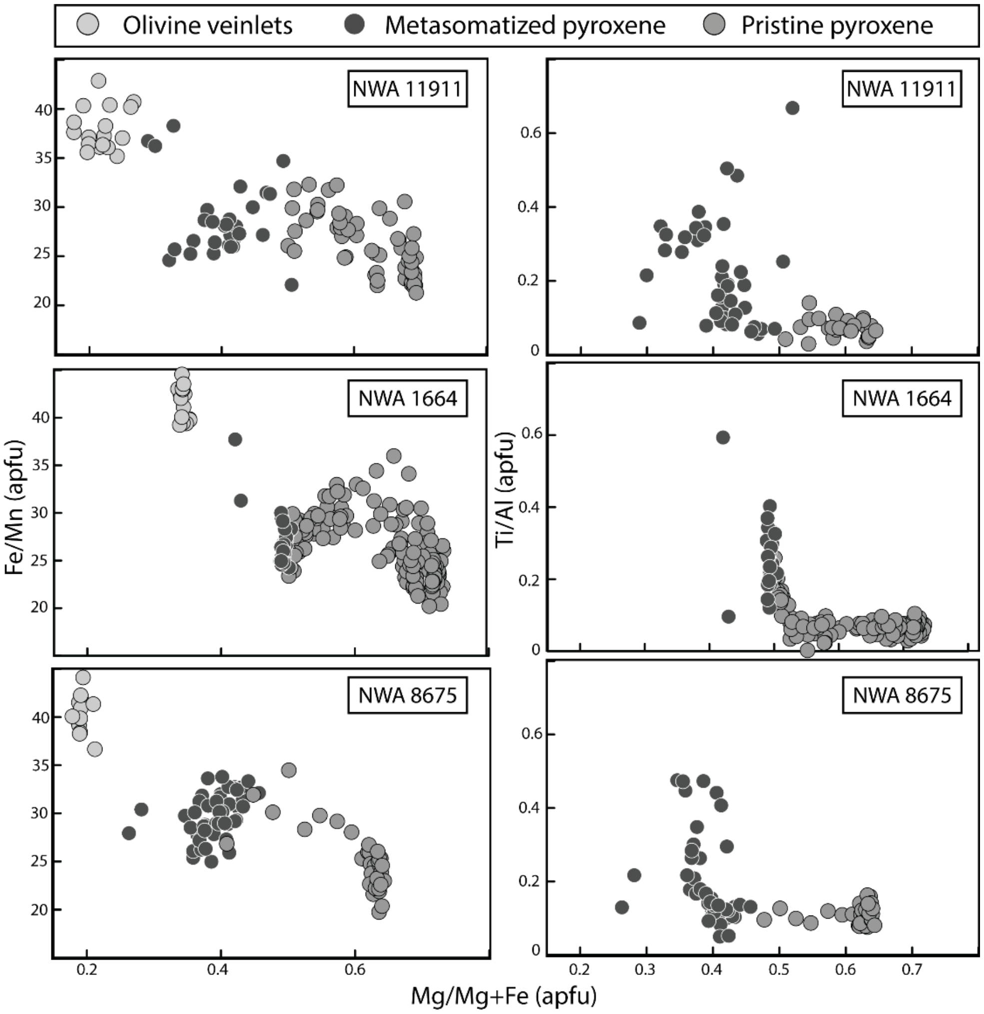

Fig. 11. Ti/Al (apfu) and Fe/Mn versus Mg/(Mg+Fe) in pyroxene of NWA 11911, NWA 1664 and NWA 8675. Note that the most Mg-rich compositions are detected in NWA 1664.

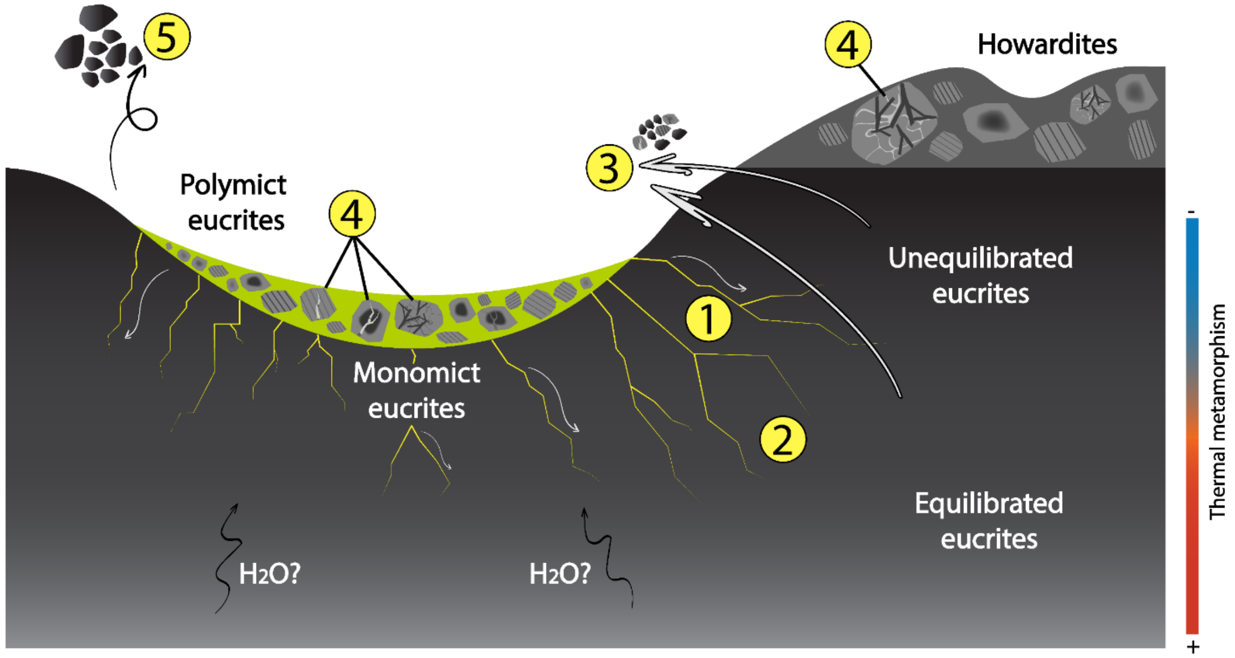

① Circulation of fluids within preexsisting cracks in unequilibrated eucrites and formation of secondary fayalitic veinlets.

② Circulation of fluids within preexsisting cracks in equilibrated eucrites and formation of secondary fayalitic veinlets.

③ Collisional events exposing and mixing unequilibrated and equilibrated eucritic material comprising secondary features.

④ Metasomatized, unequilibrated and equilibrated basaltic clasts and pyroxene fragments incorporated in the final breccia (polymict eucrites and howardites)

⑤ Ejection of various lithologies by further impacts. This includes the NWA 11911, NWA 1664, NWA 8675 and NWA 13269.

Fig. 12. Illustration showing the stages of the formation of Fe-rich, metasomatic features in eucritic material from Vesta. The source of fluids may have been endogenic due to magma degassing (black arrows; Sarafian et al. 2017) or exogenous, released during a collision between a water-rich impactor and Vesta (grey arrows; Warren et al. 2014).

ONLINE SUPPLEMENT

This supplementary document provides further support to our findings from NWA 11911, NWA 1664, NWA 8675 and NWA 13269. We present SEM images of NWA 11911 and NWA 13269 to describe their petrographic characteristics. In addition, we provide more data (BSE images, EPMA-WDS maps, EDS maps and EPMA profiles) of clasts comprising olivine veinlets in NWA 11911, NWA 8675 and NWA 1664. The compositions of Mg-cores, metasomatized pyroxenes and olivine in veinlets are summarized in tables S1 and S2.

Table. S1

Summary of the compositional data of Fe-enriched pyroxene in NWA 11911.

			Ti/Al		Mg/Mg+Fe		Fe/Mn	
NWA 11911	Mg-core	Fe-enriched px	Mg-core	Fe-enriched px	Mg-core	Fe-enriched px	Mg-core	Fe-enriched px
Unequilibrated Fragments	En_{58-63} Fs_{32-35} Wo_{3-6}	En_{37-38} Fs_{56-60} Wo_{3-6}	0.1-0.16	0.06-0.3	0.63-0.41	0.66-0.38	30-33	29-33
Basaltic Clast	En_{55} Fs_{37} Wo_{8}	En_{42} Fs_{55} Wo_{3}	0.09	0.1	0.59	0.42	27	34
Cumulate clast	En_{61} Fs_{33} Wo_{6}	En_{40} Fs_{54} Wo_{6}	0.06	0.1	0.64	0.43	29	32
Equilibrated fragments (f)	En_{48-49} Fs_{45-46} Wo_{4-5}	En_{39-42} Fs_{55} Wo_{3-6}	0.6	0.5	0.5	0.4	31	32
Equilibrated fragments (e)	En_{51} Fs_{43} Wo_{6}	En_{42} Fs_{52} Wo_{6}	0.14	0.12	0.54	0.44	31	33

Table. S2

Summary of the compositional data of pyroxenes crossed by fayalitic veinlets in NWA 11911, NWA 1664 and NWA 8675.

			Ti/Al		Mg/Mg+Fe		Fe/Mn			
NWA 11911	Mg-core	Fe-enriched Px	Mg-core	Fe-enriched Px	Mg-core	Fe-enriched Px	Mg-core	Fe-enriched Px	Olivine in veinlets	Secondary plagioclase
Unequilibrated Fragments	En_{61} Fs_{34} Wo_{5}	En_{39} Fs_{58} Wo_{3}	0.06	0.19	0.64	0.4	27	31	Fa_{72-77}	$An_{97.40}$
Equilibrated fragments	----	-----	0.3		0.38		34		Fa_{75-80}	-
NWA 1664										
Unequilibrated Fragments	En_{70} Fs_{28} Wo_{2}	En_{42} Fs_{57} Wo_{1}	0.1	0.09	0.7	0.42	28	36	Fa_{64-66}	$An_{97.96}$
NWA 8675										
Unequilibrated Fragments	En_{60} Fs_{35} Wo_{5}	En_{28} Fs_{71} Wo_{1}	0.13	0.2	0.63	0.28	24	35	Fa_{78-80}	$An_{98.00}$

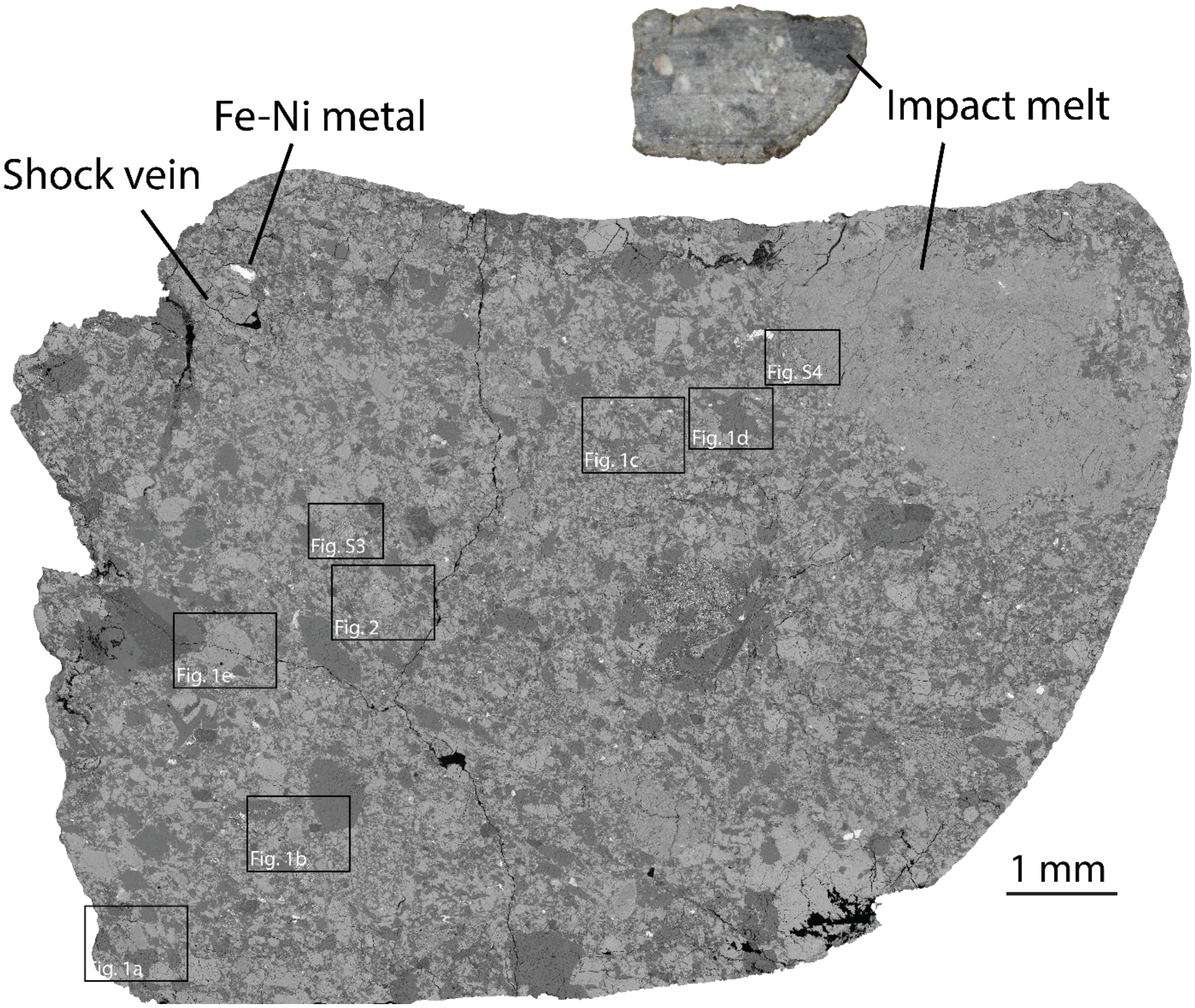

Fig. S1. SEM mosaic map of NWA 11911 showing its brecciated nature. The photograph (top right of the figure) shows the occurrence of mineral fragments and a large dark inclusion within a grey, well-cemented matrix. Note the large impact melt inclusion on the upper right of the map.

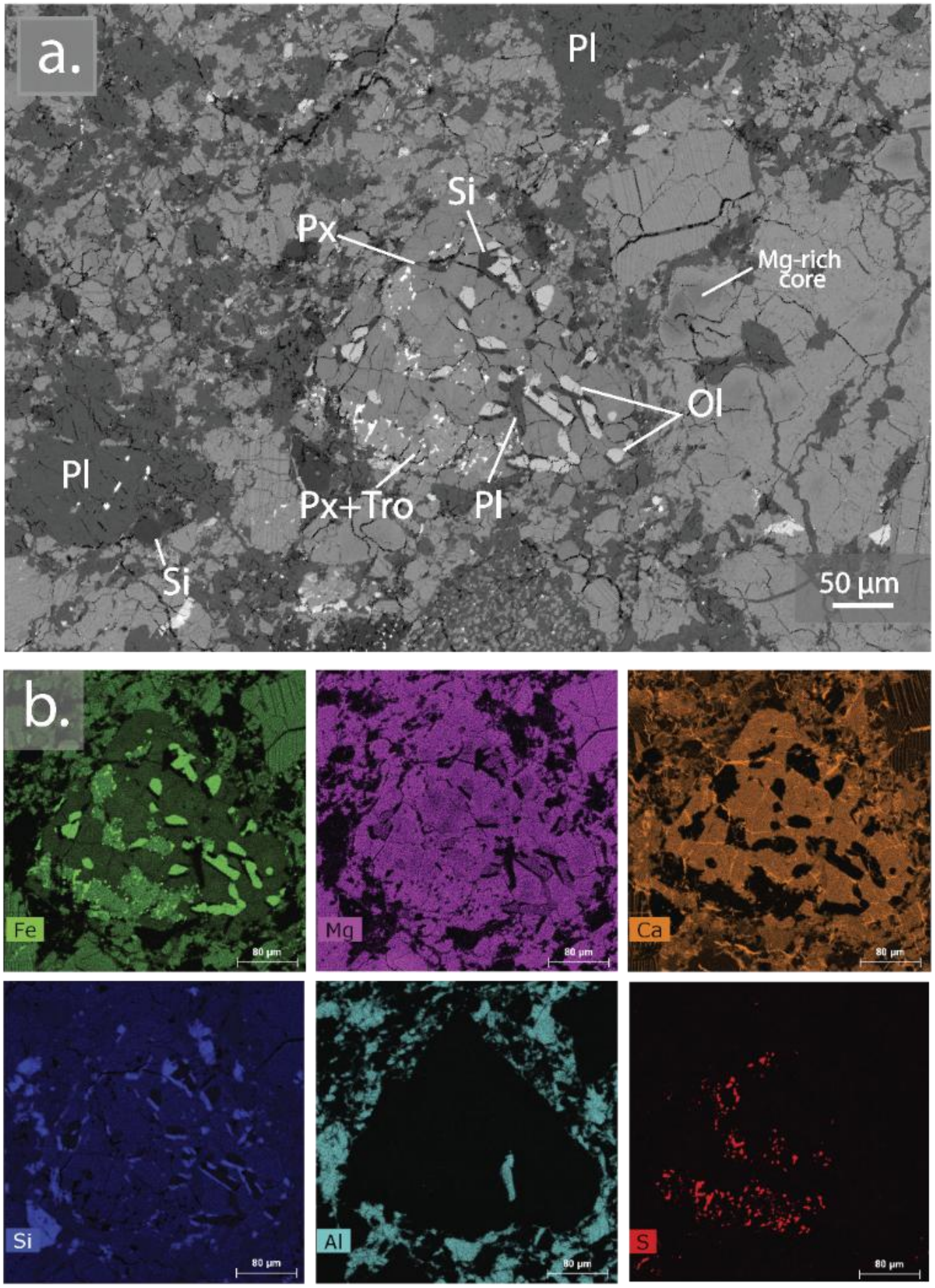

Fig. S2. SEM image of a late-stage clast in NWA 11911. The clast mainly consists of stubby olivine and silica lamellae. Note the presence of areas comprising Fe-rich pyroxene, troilite and olivine (see S map in b.). Px = pyroxene; Pl = plagioclase; Tro = troilite; Si = silica.

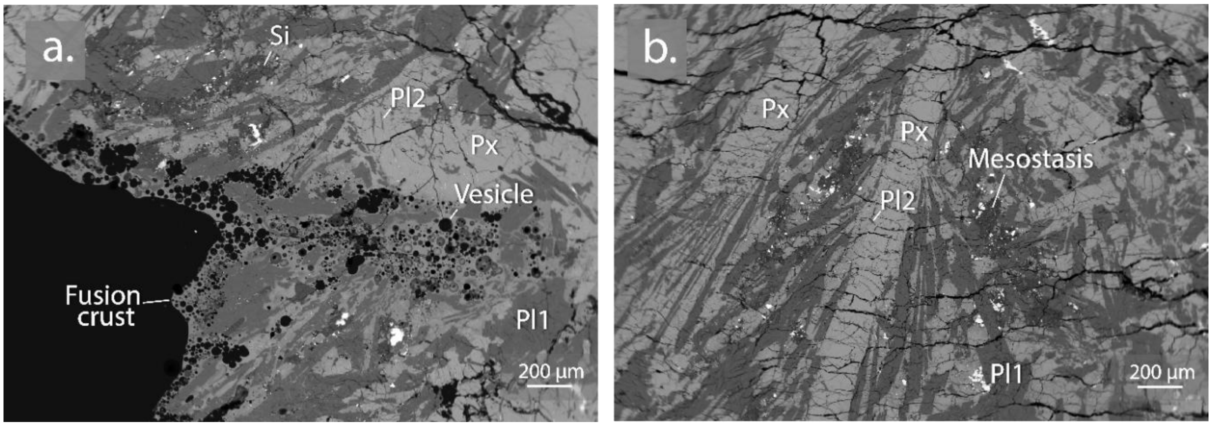

Fig. S3. SEM images of NWA 13269. (a) The fusion crust is up to 100 µm in thickness and contains abundant vesicles. In this particular area, vesicles are penetrating the interior of the meteorite by a distance of 1 mm. (b) Elongated pyroxene phenocrysts embedded in a fine-grained, subophitic to variolitic groundmass. Px = pyroxene; Pl1 = primary plagioclase; Pl2 = secondary plagioclase; Si = silica.

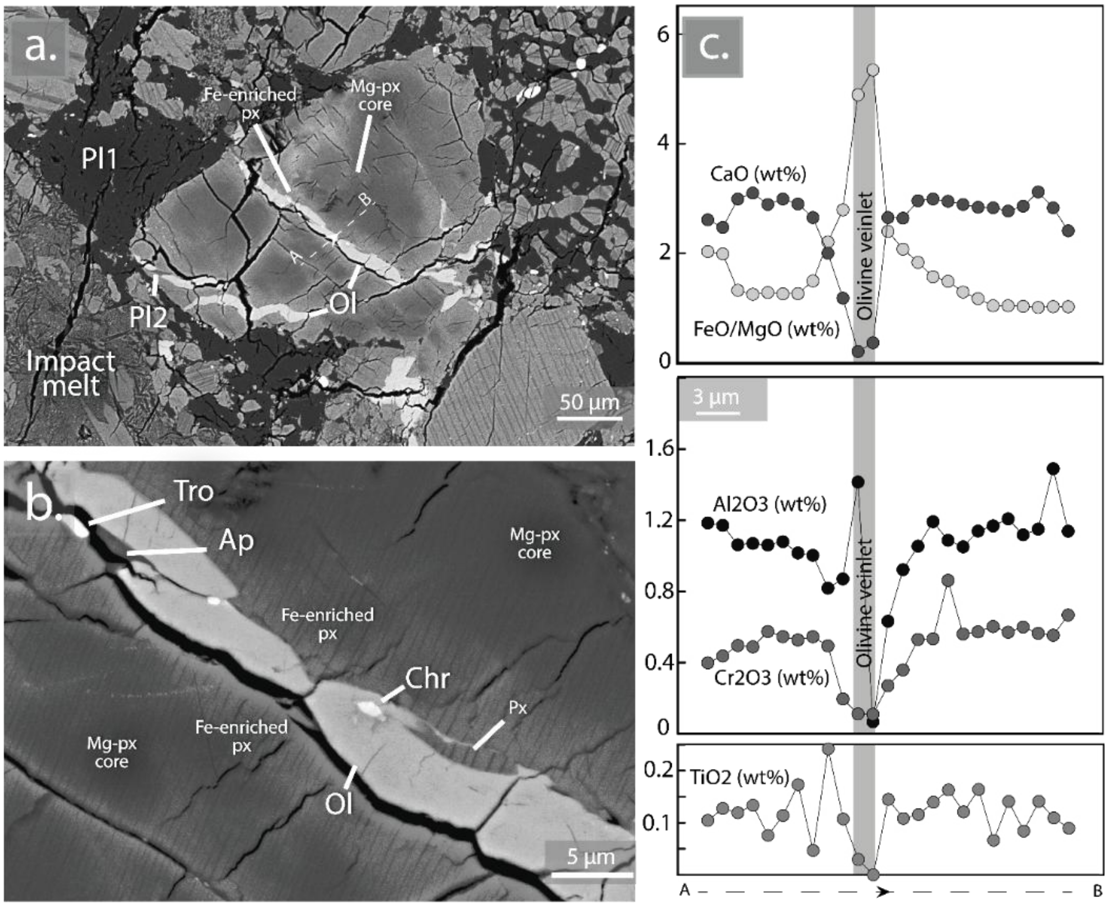

Fig. S4. SEM images and EPMA profiles (marked A-B in a.) of secondary olivine veinlets associated with Ca-rich plagioclase, Cr-spinel, troilite and apatite in NWA 11911. (b) is a close-up view of the center of the fragment. Note the presence of pyroxene within the veinlet. Ol = olivine; Px = pyroxene; Pl1 = primary plagioclase; Pl2 = secondary plagioclase; Chr = chromite; Tro = troilite, Ap = apatite.

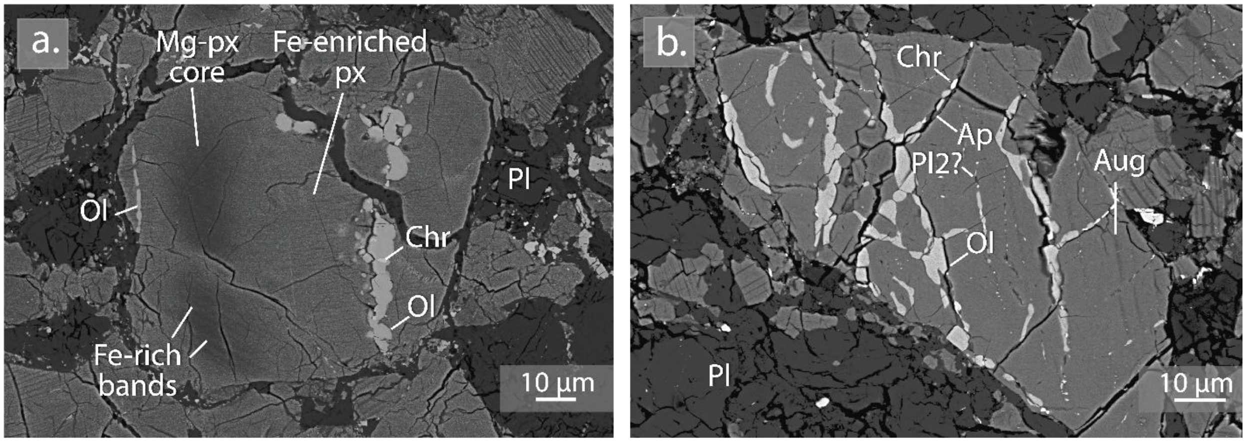

Fig. S5. BSE images of texturally different olivine veinlets in NWA 11911. **(a)** Aggregates of olivine associated with Cr-spinel. **(b)** Interconnected olivine veinlets filling cracks in slightly equilibrated pyroxene fragment. Associated phases are Cr-spinel and apatite. Ol = olivine; Px = pyroxene; Pl = primary plagioclase; Pl2 = secondary plagioclase; Chr = chromite; Ap = apatite.

Fig. S5a shows a pyroxene fragment (~100 µm in size) crossed by a 6-µm-thick fayalitic veinlet associated with Cr-spinel (2 µm across). The Mg-core has a composition $En_{56}Fs_{37}Wo_7$, and is crossed by multiple, parallel Fe-rich bands. Pyroxene adjacent to the veinlet is $En_{38}Fs_{56}Wo_6$. The composition of olivine is Fa_{80}. Note the Fe-enrichment of pyroxene along the crack crossing the Mg-core (center of the image). Fine high-Ca pyroxene lamellae (< 1 µm) are also observed.

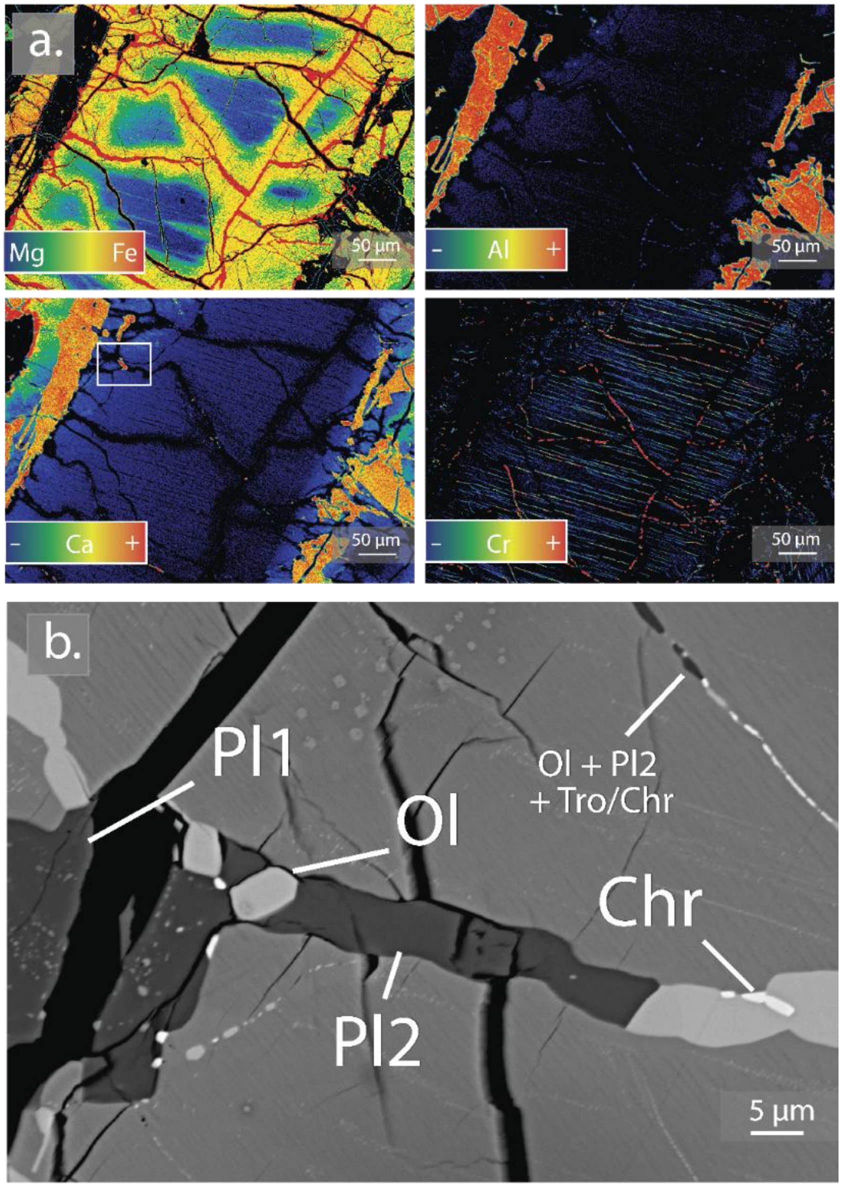

Fig. S6. EPMA-WDS maps (a) and BSE image (b) of secondary olivine veinlets crossing pyroxene in NWA 1664.

Pyroxene shown in Fig. S6a is crossed by a network of fayalitic veinlets (red color). Fe-enrichment in pyroxene is strong, and extends into pristine pyroxene by a distance of 30 µm. Al-depletion in pyroxene adjacent to veinlets is observed. Note the occurrence of parallel, 2-µm-thick chromite lamellae in pyroxene. Fig. S6b shows a 5-µm-thick veinlet consisting of fayalitic-olivine and secondary plagioclase, plus minor Cr-spinel and troilite. Ferroan olivine filling the fracture in pyroxene occurs as subhedral grains or as a continuous veinlet. The 1-µm-thick veinlet (upper right of the image) consists of olivine, secondary plagioclase and troilite or chromite. The direction of the veinlet is parallel to the direction of Ca-rich exsolution lamellae.

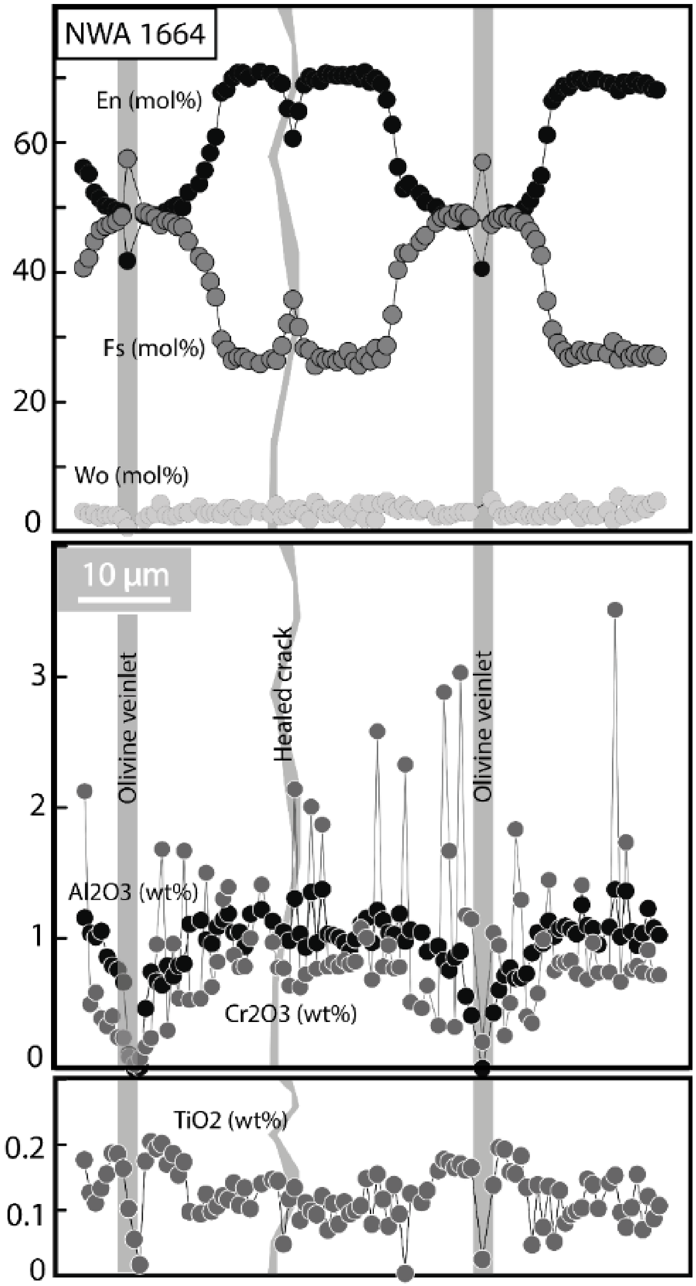

Fig. S7. EPMA profile across Fe-enriched pyroxene, a healed crack, a fayalitic veinlet and a Mg-core in NWA 1664. Note the Al-depletion near the veinlets.

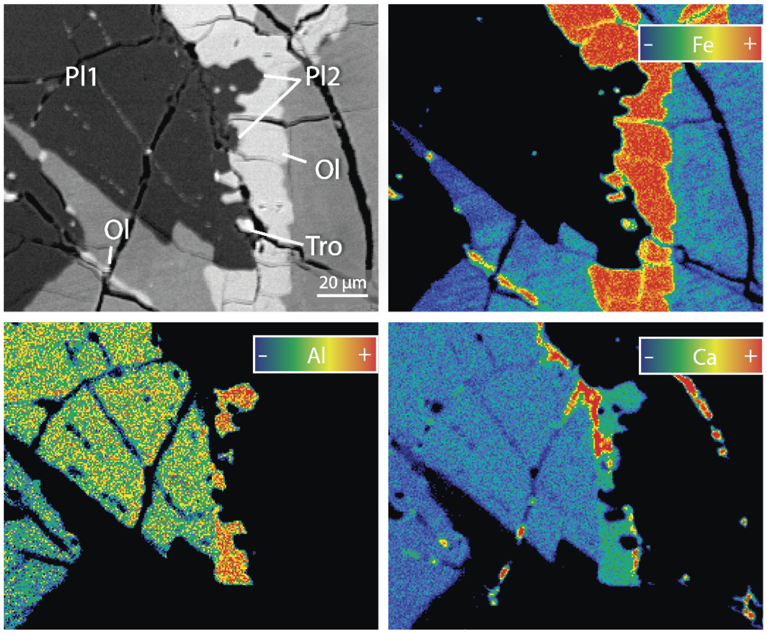

Fig. S8. SEM and EPMA-WDS maps of a fayalitic veinlet within pyroxene and plagioclase boundary in NWA 8675. Secondary, Ca-rich plagioclase here occurs as discontinuous veinlet adjacent to primary plagioclase.

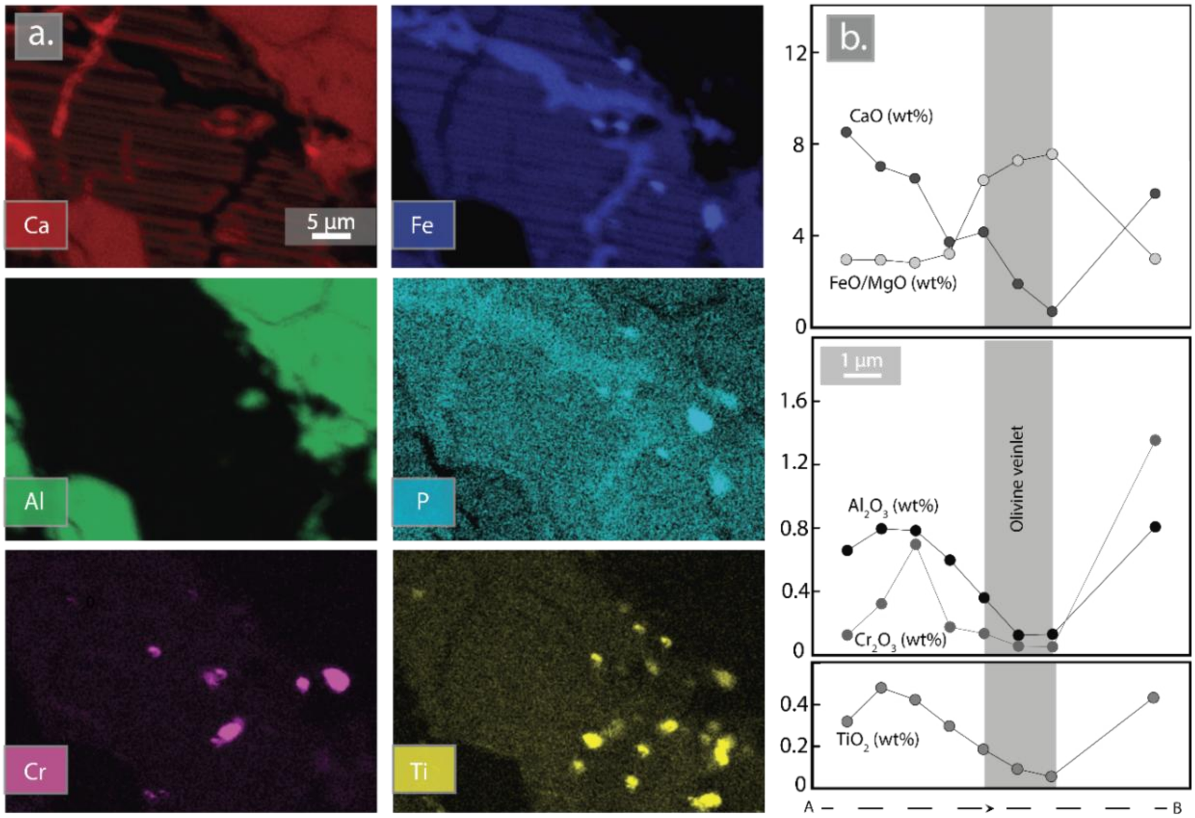

Fig. S9. EDS maps (a) and EPMA profile (b) across a fayalitic veinlet crossing an equilibrated pyroxene fragment in NWA 11911.

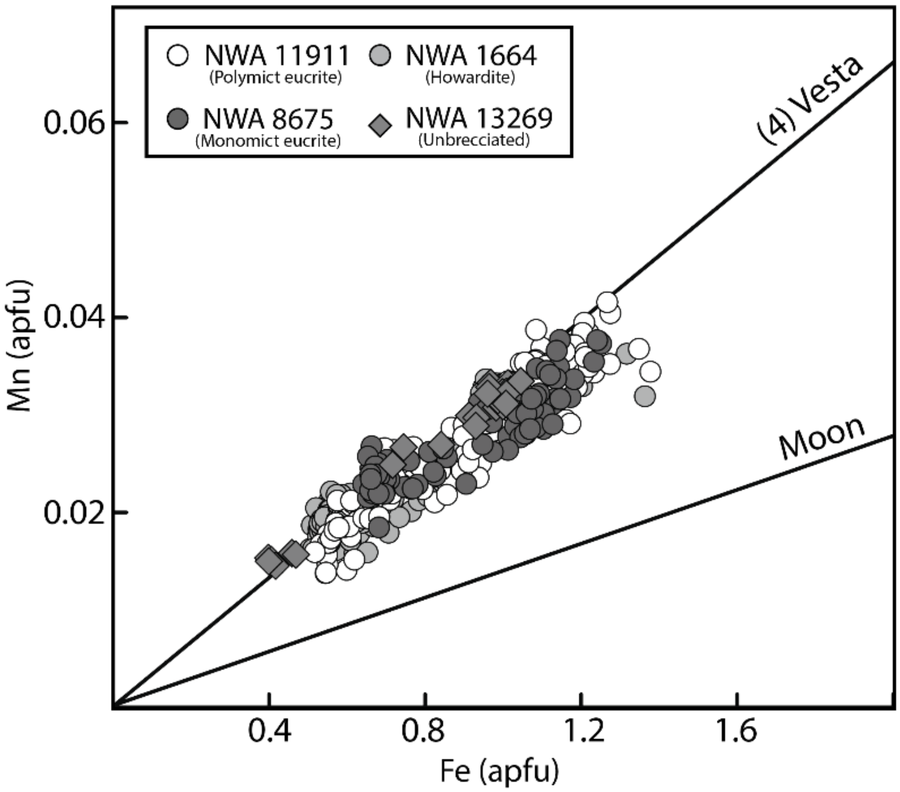

Fig. S10. Fe/Mn (Atom per formula unit – apfu) of NWA 11911, NWA 1664, NWA 8675 and NWA 13269.